Title: Aerial-aquatic robots capable of crossing the air-water boundary and hitchhiking onto surfaces

Authors:

Lei Li,[1]† Siqi Wang,[1]† Yiyuan Zhang,[2]† Shanyuan Song,[1]† Chuqian Wang,[1] Shaochang Tan,[3] Wei Zhao,[1] Gang Wang,[1] Wenguang Sun,[1] Fuqiang Yang,[1] Jiaqi Liu,[1] Bohan Chen,[1] Haoyuan Xu,[1] Pham Nguyen,[4] Mirko Kovac,[4,5] Li Wen[1]*

Affiliations:

[1]School of Mechanical Engineering and Automation, Beihang University, China.
[2]School of General Engineering, Beihang University, China.
[3]School of Automation Science and Electrical Engineering, Beihang University, China.
[4]Imperial College London, London, UK.
[5]Materials and Technology Centre of Robotics, Swiss Federal Laboratories for Materials Science and Technology (Empa), Switzerland.

*Corresponding author. Email: liwen@buaa.edu.cn
† These authors contributed equally to this work.

Abstract: Many real-world applications for robots, such as long-term aerial and underwater observation, cross-medium operations, and marine life surveys, require robots with the ability to move between the air-water boundary. Here, we describe an aerial-aquatic hitchhiking robot that is self-contained for flying, swimming, and attaching to surfaces in both air and water and that can seamlessly move between the two. We describe this robot's redundant, hydrostatically enhanced hitchhiking device, inspired by the morphology of a remora (*Echeneis naucrates*) disc, which works in both air and water. As with the biological remora disc, this device possesses separate lamellar compartments for redundant sealing, which enables the robot to achieve adhesion and hitchhike with only partial disc attachment. The self-contained, rotor-based aerial-aquatic robot, which has passively morphing propellers that unfold in the air and fold underwater, can cross the air-water boundary in 0.35 seconds. The robot can perform rapid attachment and detachment on challenging surfaces both in air and under water, including curved, rough, incomplete, and biofouling surfaces, and achieve long-duration adhesion with minimal oscillation. We also show that the robot can attach to and hitchhike on moving surfaces. In field tests we show that the robot can record video in both mediums and move objects across the air/water boundary in a mountain stream and the ocean. We envision that this study can pave the way for future robots with autonomous biological detection, monitoring, and tracking capabilities in a wide variety of aerial-aquatic environments.

One-Sentence Summary: A self-contained robot that can swim, fly, and attach to surfaces across air and water

This document is the accepted manuscript version of the following article:
Li, L., Wang, S., Zhang, Y., Song, S., Wang, C., Tan, S., … Wen, L. (2022). Aerial-aquatic robots capable of crossing the air-water boundary and hitchhiking on surfaces. Science Robotics, 7(66), eabm6695 (13 pp.). https://doi.org/10.1126/scirobotics.abm6695

Main Text:

INTRODUCTION

Robots are used in place of human beings to execute missions in extreme environments, such as deep-sea exploration (*1-3*), space operations (*4*), and subterranean monitoring (*5*). Aerial robots, in particular, are widely used in outdoor environments for locating pollution sources, tracking wildlife, and monitoring biodiversity (*6-8*). Many related activities, including disaster first-response, nuclear power infrastructure surveys, and coastal patrols, require robots to transit and operate in both air and water (*9, 10*, *11*). Robots that can operate across different environments have been reported in a few studies (*12-22*); however, an untethered robot with the ability to execute stable, rapid, and consecutive transit between the air and water has not yet been described. A robot that could seamlessly do so would greatly expand the capabilities of existing human-made machines. Such robotic forms may be promising for several open-environment applications, including long-term air and water observation, cross-medium operations, submerged structure inspection, marine life surveys, iceberg detection, and more (Fig. 1).

Long-term robotic missions that require continuous flying or underwater propulsion can consume an enormous amount of power. A "rest" mode, enabled by a perching device, could allow a robot to remain in a stationary state and spend less power during an observational task (*23*). Previous perching devices include modularized landing gear (*24*), active or passive grippers (*25, 26*), gecko-inspired dry adhesives (*27*), suction cups (*28*), microspines (*29, 30*), magnets (*31*), and electrostatic adhesion (*23*). However, these adhesive structures typically fail to attach well to slippery underwater surfaces and are difficult to resist the robot body's drag under fast shear flow. Thus, a "hitchhiking" apparatus that functions both in air and under water would substantially enhance the aerial-aquatic robot's performance.

There are two primary challenges to implementing this robot with the ability to perform aerial-aquatic hitchhiking: it requires a reversible, adaptable, powerful, and robust adhesive device that functions both in air and under water, allowing the robot to hitchhike on various surfaces; and an untethered platform that can rapidly and seamlessly cross the air-water boundary.

To address the challenge of the hitchhiking device, in this article we look to nature for inspiration for a biological attachment system (*32-34*). Some of these sources of inspiration for cross-medium adhesion are highlighted in Fig. S1. However, a biomimetic study of cross-medium and multi-terrain "hitchhiking" in nature is still lacking and not well studied. Remoras, which have attracted growing attention recently (*35-42*), can hitchhike on fast-moving marine hosts (such as sharks, whales, marlins, and human divers) to reduce their energy consumption. The remora's hitchhiking ability derives from the adhesive disc located on the dorsal side of its head. In an earlier study, with a tethered, 3D-printed, pneumatic actuated biomimetic disc, we summarize the remora's adhesion mechanism as the soft disc lip forms a seal and results in a pressure differential with the outside environment, and the spinules enhance the disc's friction to overcome the shear flow force (*36, 40*). Interestingly, photographers and researchers have discovered that remoras can remain firmly attached to dolphins that spin in the air while attempting to remove their parasites (Fig. 2A). We were intrigued that the remora's disc functions not only under water but also in air, adding to previously described single-medium adhesive mechanisms such as the gecko's van der Waals force (*43*) and the tree frog's capillary

force (*44*). We also found that a live remora can attach to a porous surface with only part of its disc (Fig. 2B, Movie S1). More surprisingly, an anesthetized remora can successfully hang in the air from a glass substrate using just one-half or one-third of its disc (Fig. S2A). The redundant, adaptable adhesion of the remora in both air and water encourages us to investigate the morphology of its disc more carefully. Additionally, conventional suction devices are sensitive to leakage and external impact. Implementing a bioinspired adhesive device that is highly adaptable, frictional, and robust is essential for robots to hitchhike onto various surfaces in both air and water.

To address the challenge of the seamless aerial-aquatic transition, the robot needs to perform untethered, rapid, and consecutive transits between the air and water and move stably in the two media. A few forms of aerial-aquatic robots have been developed previously, including fixed-wing (*13-15*), foldable wing (*16, 17*), flapping-wing (*18*), rotor-wing (*19-21*), and hybrid fixed-rotor-wing (*22*) forms. In this study, we chose the rotor-wing form to develop a robot due to its stability, low cost, and ease of operation. Previously described rotor-form robots have performed aerial-aquatic transitions (*19-22*). For example, the robot presented by Maia et al. is a tethered device with a limited operating domain in the field (*19*). Moreover, Alzubi et al. (*20*) and Lu (*22*) et al. introduced rotor-based robots capable of air/water transitions with the help of buoyancy devices, which resulted in relatively long transition times (13 s and 30 s, respectively) (Table S1). To achieve a rapid transition, a robot's air-water crossing period should be shortened as much as possible. A rotor-based robot needs to expose its propellers above the water surface and rapidly accelerate them to a high rotational speed to generate enough force to lift the robot out of the water.

This study aims to develop a robot that can perform a seamless aerial-aquatic transition and hitchhike onto complex surfaces in both air and water. First, we analyzed the morphological features of the redundant adhesive mechanism of the biological remora's disc. Then we implemented an onboard-actuated, redundant biomimetic adhesive device based on the fundamental principles of the remora disc. With the biomimetic disc, we also studied the effects of morphological features on the redundant adhesive performance both in air and under water. Then, we introduce the self-contained aerial-aquatic hitchhiking robot with morphing propellers, which passively unfold in the air and fold under water. This robot can be remotely controlled for flying, swimming, and attaching to a wide range of surfaces in air and water and seamlessly transition between the two. Finally, we characterize the robot's performance and demonstrate its application in the field.

RESULTS

Morphological features of the biological remora disc's redundant adhesion

Using a high-speed camera, we observed a living remora fish (*Echeneis naucrates*, 280 mm long and 30 mm wide) attaching to a porous acrylic surface on the side of an aquarium from a dorsal point of view (Movie S1). As shown in Fig. 2B, we found that even if a few segments of the adhesive disc are located above the holes (20 mm in diameter), which causes the seal to leak, the remora can still attach to the acrylic surface with the rest of its disc. We also demonstrated that a deeply anesthetized remora could adhere to a substrate using only a portion of its disc (Fig. S2A). We applied Frustrated Total Internal Reflection (FTIR) to visualize the contact status between an anesthetized remora's disc and a transparent substrate (Fig. 2C and Movie S2). The green fluorescent section indicates the contact area between the disc and the substrate, and the black section indicates no contact. The dotted-line frame represents a single lamellar compartment

composed of two rows of adjacent lamellae and the surrounding fleshy disc lip. In an entire adhesive disc, there are 24 rows of disc lamellae that form 25 lamellar compartments that form independent seals with the surface. Thus, it is evident that the remora' disc has a unique feature: adhesion redundancy.

To investigate the morphological features that facilitate the partial adhesion of the disc, we utilized a micro-computed tomography (micro-CT) to scan the head of a remora specimen. This approach enables the digital reconstruction of both the specimen's bony and soft tissues. From the cross-sectional micro-CT image (Fig. 2D), we observed that the remora disc includes lamellae soft tissue (orange), lamellae bony structures (white), connective tissue (yellow), a disc lip (earthy yellow), muscles for actuating the lamellae (green), and blood vessels (red). Our previous studies of remora models indicate that the soft lip functions as the seal (*36, 40*) and rotatable lamellae covered with soft tissue and sharp spinules enhanced friction (*36*). Here, we observed several morphological features that may contribute to disc adhesion: the connective tissue between the disc lip and lamellae, the passive compliance of the lamellae, and the compliant muscles and vessels below the adhesive disc structure.

The main morphological features of the disc that form independent lamellar compartments are the soft tissue connected to the lamellae and the soft lip; and the flexible lamellae can be passively rotated and have a tilted angle on top. These two features facilitate redundant adhesion. Using a light microscope and tissue section staining, we observed connective tissue (thickness of around 500 μm, Fig. S3) that joins the lamellae soft tissue with the fleshy disc lip. Figure 2E shows this connective tissue from a recently euthanized remora manipulated with tweezers (Movie S3). To date, little attention has been paid to the connective tissue of the remora disc, but this morphological feature is essential for forming the redundant seal of the disc. We also constructed a 3D model of the bony structure of a single lamella (Fig. 2F), and noticed an angle between the lamella's top surface relative to a flat surface ($\beta = 18.36 \pm 3.08$ deg, $N = 12$ trials, error bars represent ± 1 SD). The soft muscles and vessels underneath the adhesive disc enable oblique lamellae (α) to rotate passively (see Movie S3), which causes adaptive engagement with the environmental surface during adhesion. In addition, we found that the biological adhesive disc is flexible and can bend to attach to curved surfaces (Figs. S2B and S2C). In the following section, we will investigate the effects of these morphological features on the adhesion of lamellar compartments through a biomimetic robotic prototype.

Biomimetic disc with redundant, hydrostatically enhanced adhesion

Based on the morphological features of the natural remora disc, we designed and fabricated a biologically-inspired prototype that has independent lamellar compartments for a redundant seal (Fig. 3A, Fig. S4-7, Movie S4). The prototype (87 mm long and 46 mm wide; 36.2 g weight) allows a systematic investigation of the remora's self-adaptive, redundant, and hydrostatically enhanced adhesive mechanism by testing isolated morphological features. The biomimetic disc consisted of four functional layers: a thin ultra-soft layer to connect lamellae to the disc lip; a multi-material 3D-printed main disc; a thin fluidic actuated microchannel network layer for rotating the lamellae (Fig. S5A); and a soft fluidic actuator strengthened by fibers for bending the disc (Fig. S5B). A soft layer (elasticity modulus of 55 kPa) connects the lamellae and disc lip, mimicking the biological connective tissue and enabling redundant adhesion. This soft layer also allows the biomimetic disc to form a robust seal on a wide range of surface asperities. Inspired by the remora's lamellae muscles and large cranial veins, we implemented a flexible hydrostatic

chamber network that performs the functions of both the lamellae muscle and cranial vein (which induces hydrostatic force). The flexible hydrostatic chamber network enables erecting and depressing each row of lamellae with stainless steel spinules (Movie S4). Additionally, fibers reinforcing the soft actuator enable the disc prototype to bend when pressurized hydraulically (Fig. S9A, Movie S4).

Contact surface measurements show that the biomimetic disc can form independent lamellar compartments and achieve redundant adhesion just like its biological counterpart. Fig. 3B shows that the biomimetic redundant disc formed nine lamellar compartments when attaching to smooth, transparent glass. Even after externally imposed leakages broke three seals, the disc remains stably attached using the rest of its sealed compartments. In contrast, the disc prototype without redundancy immediately detached after sustaining only one leak (Fig. 3C, Movie S5). The morphological features and functional performance of the current biomimetic disc versus those of the previous bioinspired remora disc (*36*) are compared in Table S2.

To elucidate the working principle of the adhesive device, shown in Figs. 3D-3F, we divide the adhesive process of the device into three stages: pre-contact; self-adaptive, redundant adhesion; and frictional enhancement by hydrostatic pressure. During initial adhesion (Stage one, Fig. 3D), the disc contacts the environmental surface ($P_{1I} = P_{2I} = P_0$). Next (Stage two, Fig. 3E), the external preload presses the disc onto the surface, causing an engagement with the substrate. Due to the oblique lamellae (α) and the soft nature of the flexible hydrostatic chamber, the biomimetic lamellae can passively rotate during contact. Meanwhile, the lamellae's ventral process presses on the flexible hydrostatic chamber, causing fluid to flow toward the external actuator chamber. The composite lamellae, covered with soft material on top and attached to the disc lip via connective tissue, form a tight seal with the substrate. When the preload imposed on the disc is removed, the stored elastic energy of the disc's soft material allows the lamellae to rotate back toward their original angle, forming a pressure differential between the compartments and the external environment that achieves a stable adhesion ($P_{1II} < P_0$, $P_{2II} < P_0$).

During the enhanced frictional stage of adhesion (Stage three, Fig. 3F), the external soft actuator chamber is compressed or squeezed, causing fluid to flow back to the lamellae chamber. The hydrostatic expansion of the lamellae chamber further rotates the lamellae (in a counterclockwise direction), causing the spinules and soft material of the lamellae to engage with the environmental surface ($P_{1III} < P_{1II}$, $P_{2III} < P_{2II}$). This engagement further enhances adhesion, particularly frictional force. In Supplementary Text S1 and Fig. S8, we analyzed the relationship between the internal pressure of the lamellar compartment (P_k) and the disc's adhesive force (F_a). In the enhanced adhesion stage, the decrease of internal pressure of the lamellar compartment (P_k) caused the increase in the disc's adhesive force (F_a).

The suction disc's flexible lamellae can be passively rotated and have a tilted angle on top. We provide a geometric model of the oblique lamellae while contacting the substrate (see Fig. S9B, and Supplementary Text S2). We experimentally show that the passively rotatable lamellae with an angled top improve the adaptability of the redundant adhesion (Fig. S9C and S9D). The modulus of the disc's soft layer on top also played a role in facilitating the redundant adhesion (Fig. S9E, and Supplementary Text S3). The internal pressure of one single lamellar compartment showed that erecting the lamellae through

external actuation can strengthen the independent compartment's adhesion and enhance the frictional force without breaking the compartment's seal (Fig. S9F).

Adhesion performance of the biomimetic redundant disc in air and water

We found that biomimetic redundant adhesive discs formed redundant adhesion with different rows of lamellae (Fig. 4A). We show that contact surfaces of four adhesive discs with 2, 4, 6, and 8 rows of lamellae formed 3, 5, 7, and 9 lamellar compartments, respectively, with a preload force (20 N). Fig. 4B shows that the frictional stress of the biomimetic disc increases with the number of lamellar compartments. Notably, the frictional stress of the disc with 8 lamellae increased by 73.4% (in the air) and 22.0% (underwater) compared to the disc with 2 lamellae. The frictional stress of the disc with 8 lamellae increased by 1.3% (in the air) and 0.9% (underwater) compared to the disc with 6 lamellae. The increase in frictional stress became less obvious with additional lamellae rows.

We compared the frictional force of the fully functional biomimetic disc with hydrostatic enhancement (orange line); disc control without lamellae compliance (yellow line, tilted and non-compliant); disc control without lamellae compartments (blue line); and biomimetic disc with lamellae compartments and compliance, but without hydrostatic enhancement (grey line), on an experimental surface (R_a = 50 μm: grain size of sandpaper) both in air and under water (Figs. 4C and 4D). The results of the maximum static frictional stress are shown in Fig. 4E. The frictional stresses of the biomimetic prototype are 44% (air, dashed grey line) and 15% (under water, solid grey line) greater than that of the control (without lamellae compartments, compartments were connected by small holes, blue). The self-adaptive lamellae induced notably greater frictional stress (61% in air, 30% in water, grey) than the non-self-adaptive lamellae (where the lamellae were constrained in their rotational axis, yellow). We also noted that the soft hydrostatic chamber raised the lamellae, enhancing the frictional stress (orange) up to 42.9 ± 2.1 kPa (134.9 ± 6.6 N, under water) and 32.3 ± 1.8 kPa (101.4 ± 5.6 N, air), corresponding to increments of 41% and 56% compared with the disc without hydrostatic enhancement (grey).

To show the redundant adhesive performance induced by the lamellar compartments of the biomimetic disc, we tested the pull-off force of the disc with only a few lamellar compartments (the middle three lamellae) on surfaces of different roughnesses (Fig. 4F). The pull-off forces generated by the three lamellar compartments ranged from 17.4 ± 2.5 N on a smooth surface to 6.3 ± 1.2 N on a rough surface in air and from 63.9 ± 1.9 N to 23.0 ± 2.8 N under water. The lamellar compartments had the maximum adhesion stress of 13.8 ± 1.9 kPa (air) and 50.8 ± 1.5 kPa (under water) on the smooth surface. The maximum surface roughness these three lamellar compartments could attach to was 50 μm (in air) and 269 μm (under water).

The frictional stress generated by the biomimetic disc is notably greater than that of the control group (without lamellar compartments) on different rough surfaces both in air and under water (Fig. 4G). The maximum frictional stresses of the biomimetic disc generated on the smooth surface were 24.3 ± 0.5 kPa in air and 33.2 ± 0.6 kPa under water. The maximum increase of the frictional stress by the biomimetic disc is 44% (50 μm, air) and 15% (50 μm, under water) greater than that of the control. The biomimetic disc can achieve a frictional stress of 19.2 ± 0.4 kPa on a surface with high roughness (R_a = 764 μm).

We further measured the adhesion time of the biomimetic disc and the control disc (without lamellar compartments) under different vertical external loads on a rough surface (50 μm) both in air and under water (Fig. 4H). The results show that the biomimetic prototype with lamellar compartments has a maximum adhesion time of 2944.4 ± 143.7 min (load of 10N, under water), which is 206% greater than that of the control disc. We also tested the disc under an external load of 30N: the biomimetic disc stayed robustly attached for 400.7 ± 55.6 min (under water) and 94.8 ± 12.5 min (air), which are 150% and 458% greater than the times recorded for the control disc, respectively. Because the adhesion failure of the disc is mainly caused by suction leakage, the redundant adhesion through lamellar compartments can maintain a seal even with partial leakage, thus notably increasing the adhesion time.

Adhesion force decreases as surface roughness increases (Fig. 4I). The biomimetic disc produced the maximum adhesion stress of 39.6 ± 0.5 kPa (124.4 ± 1.6 N, air) and 69.6 ± 0.5 kPa (218.9 ± 1.7 N, under water) on the smooth surface. The maximum roughness of the rough surfaces that the disc could attach to were about 425 μm (in air) and 764 μm (under water), respectively.

We also show that the biomimetic disc can attach to curved surfaces of different radii (20 mm, 35 mm, 50 mm, 70 mm) (Fig. 4J). The maximum normalized curvature (u) that the biomimetic prototype can attach to is 2.18 ($u = R_d / R_s$, where R_d represents the length of the semi-major axis of the elliptic disc, and R_s represents the curvature radius of the surface), and the adhesion stresses generated are 5.2 ± 0.2 kPa (air) and 7.1 ± 0.4 kPa (under water), respectively. Figure 4K illustrates the pull-off process of the biomimetic disc on a typical curved ($u = 0.87$) and rough (50 μm) surface, for which the maximum pull-off force is 50.3 ± 3.7 N in air and 99.6 ± 4.0 N under water.

To demonstrate the biomimetic disc's redundant, self-adaptive adhesion, we tested its performance on various objects of different sizes, shapes, weights, and surface morphologies (Fig. 4L, Movie S6). The disc shows several distinct features while grasping these objects. For example, the disc can grasp a cell phone (mass of 174 g) and goggles (32 g) with only half and one-third of the disc's surface area engaged, respectively. We also show that this device can grasp a roll of tape (134 g) and a conch shell (525 g).

The aerial-aquatic robot with self-folding propellers

We developed an untethered hybrid aerial-aquatic robot by integrating a modified quadrotor robot equipped with the biomimetic disc as a hitchhiking device (40 cm×40 cm×14 cm, overall weight: 950g), as shown in Fig. 5A. Figure S10A shows the frame of the robot's control hardware. We designed and fabricated the disc with actuation components, including two hydraulic systems for the lamellae and bending the disc (Fig. S10B), and a cable-driven system for curling the disc lip for detachment (Fig. S10C, Movie S7). The control system consists of a flight control module, an electronic governor, PPM (Pulse Position Modulation) encoder, low-frequency radio communication equipment, remote control, and battery (detailed signal transmission process in Supplementary Text S4). We used silicone rubber to waterproof the entire electrical system of the robot (Fig. S11 and S12).

In order to shorten the air-water transition period as much as possible, we designed and implemented passive morphing propellers for the aerial-aquatic robot. We installed 5-inch aerial blades (Gemfan Hobby Co., Ltd., China) on a 3D printed fixture to create propellers

with a folding ratio of 2 (Figs. S13A and S13B). While rotating, the propellers can self-fold underwater and self-unfold in the air. The aerial-aquatic robot equipped with this propeller design can take off from underwater into the air within 0.35 s (Fig. 5B, Movie S8). Figures. 5C-5E show high-speed images of the propeller passively shifting from a folded to an unfolded state during the water-to-air liftoff (Movie S8). We also show that the propellers can passively fold during the air-to-water transition process (Movie S8). The propellers' blades can be passively folded underwater as the fluid force pushes the blades inward. As such, the propellers were in a folded state (d = 85 mm) underwater (Fig. 5C). When the propellers were exposed to the air, their rotational speed rapidly increased, leading to increased centrifugal forces that unfolded all the blades (D = 170 mm) (Fig. 5D and 5E). The thrust forces of the self-folding propellers both underwater and in air at different rotational speeds are shown in Figs. 5F and 5G, respectively. The thrust forces of the other two types of propellers are provided in Fig. S14.

We compared the transition performance of robots with three types of propellers: self-folding, commercial, and self-folding propellers fixed in an unfolded state, all with the same type of blades. Fig. 5H shows the self-folding propellers' rotational speed vs. time during the robot's transition from water to air; the speeds of the other two propellers are provided in Fig. S15. The area between the two black dashed lines represents the transition process. Figure 5I compares the transition time of the robot equipped with the self-folding propellers, the commercial propellers, and the self-folding propellers fixed in the unfolded state. The results show that 35% motor throttle is required to achieve a water-to-air transition for the robots with the self-folding propeller. At this throttle, the transition took 0.69 ± 0.09 s. In contrast, the robot with fixed-unfolded propellers took 1.06 ± 0.11 s at 35% throttle. With commercial propellers, the minimal required throttle percentage for the transition was 50%, and the transition process took 1.39 ± 0.16 s. Additionally, the transitional time of the robot with self-folding propellers operating at 50% throttle was reduced by 61.1% compared to the commercial propeller. At 100% throttle, the robot with self-folding propellers only took 0.35 ± 0.01 s to complete the water-to-air transition. Across all throttle ranges, the robot's average transition time with self-folding propellers was 19.1% shorter than that for the robot with commercial propellers, and 27.3% shorter than that for the robot with fixed-unfolded propellers. For more details about the measured forces and comparative transitions, see Supplementary Text S5 and Fig. S16A.

Figure S16B illustrates the robot's center of mass trajectories as it moved from water to air. The trajectory is approximately a straight line, and the displacements of the trajectory in the x and y directions are shown in Fig. S16C (x: 6.91 cm, y: 9.09 cm), 17.3% and 22.7% of the quadrotor's length, respectively. The robot's maximum roll and pitch angles are 2.1 deg and 2.4 deg during the transitions (Fig. 5J), which could be quickly adjusted to a stable flying position once airborne. Furthermore, the robot smoothly transited a choppy water surface (Movie S9, and Supplementary Text S6).

We also show that the robot can perform consecutive transitions (Fig. 5K). The entire process includes takeoff from the water (depth of ~30 cm), a water-to-air transition, flying out of the water for a short distance (~30 cm), then an air-to-water transition, and finally diving into the water. We showed that the robot could perform 7 consecutive air-water transitions in 20.3 s, taking 2.9 s per transition on average (Movie S10). Regarding transition time alone, we measured through high-speed images that the water-to-air process took 0.43 ± 0.03 s (N = 7), while the air-to-water transition process took 0.13 ± 0.06 s (N = 7). Additionally, the robot could perform "figure eight" and "pentagram"

trajectories while remotely controlled underwater at a depth of 1.5 m (Figs. S16D and S16E, Movie S11), which demonstrates the maneuverability of the robot in an underwater environment. The combination of the redundant adhesive disc and the aerial-aquatic quadrotor brought several advantages (see Supplementary Text S7, Fig. S17, Movie S12), and the adhesive disc did not notably affect the transition time of the robot (Fig. S17G).

The results from Fig. S16F show that the robot's air-water transition (per cycle) consumed 1.9 times the power of hovering in the air. Notably, the robot's hitchhiking state can reduce power consumption up to 51.7 times (in air) and 19.2 times (under water) compared to a hovering state. The method of power measurements is provided in Supplementary Text S8.

The hitchhiking performance of aerial-aquatic robots

We systematically explored the robot's ability to hitchhike onto moving objects in air and under water with a towing tank (Figs. S18A and S18B, Movie S13). We divided the hitchhiking of a moving object of the aerial-aquatic robot into three stages: approach, contact, and attached following (Figs. 6A-C). During the approach stage (Fig. 6A), a plate moved horizontally at $v_a = 0.5$ m/s, and the robot was steered to move vertically up towards the moving plate; its initial horizontal speed is zero ($v_q = 0$). The robot overcame gravity and air/water resistance via the thrust force generated by the propellers. During the contact stage ($v_q < v_a$) (Fig. 6B), the adhesive disc hit the plate and formed a seal under the preload force of the robot. The vertical speed of the robot immediately dropped to zero. In the horizontal direction, the robot slid on the surface, away from the direction of movement, with a distance of about 15.8 mm due to the speed difference between the robot and the plate. Due to the frictional force generated by the disc, the robot stopped sliding until it reached the same speed as the host plate (Fig. 6C).

Figs. 6D and 6E show the peak vertical forces during the robot's hitchhiking process, measured as 78.6 ± 12.4 N in the air and 60.6 ± 9.5 N under water. To hitchhike, the robot needed to provide a vertical preload for the biomimetic disc to attach to the surface. Our results showed that the robot could provide sufficient force to preload the biomimetic disc (8 N required on a smooth surface and 10 N on a rough surface with $R_a = 200$ μm). The peak shear forces during the hitchhiking process were measured at 18.4 ± 8.8 N in the air and 31.6 ± 4.3 N under water. The contact stage took about 0.07 s. During the attached-following stage ($v_q = v_a$), the robot stably hitchhiked on the plate. The measured shear forces were 0.375 ± 0.69 N in the air and 4.3 ± 0.73 N under water. We also recorded peak shear forces of the robotic hitchhiking to the moving plate at 0.1 m/s and 0.3 m/s (Fig. S18C). We estimated that the maximum speed of the "host" that our robot can resist is 4.3m/s (on a 50 μm surface underwater); for more details, see Supplementary Text S9. In Fig. S19, we demonstrate that the robot could hitchhike to the moving plate (0.5m/s) with only one-half of its disc attached, demonstrating the disc's attachment redundancy (Movie S13).

We also demonstrated the robot's hitchhiking ability in a fully submerged underwater environment (Fig. 6F, Movie S13). At first (0 s), the robot is in standby mode attached to the wall of a swimming pool. When the target host (a larger underwater robot) appears, the robot quickly detaches and accelerates to hitchhike on the host (at 10 s). As it gradually approaches the bottom of the host, the robot uses its propellers to control its orientation and aligns its disc with the bottom surface of the host. The propellers provide a sufficient

preload force for the robot to attach (at 20 s). Once the attachment is complete, the robot switches back to "standby mode" (stopping power to the propellers and hydraulic systems) and "travels" with the host with minimal power consumption (at 25 s).

We show that the robot can perform underwater attachment and detachment on challenging surfaces (Movie S14). For example, Fig. 6G shows the robot's redundant adhesion ability: it can attach to a narrow acrylic surface with only half its disc. The robot can also attach to a curved, rough underwater surface by pre-bending its disc to adapt to the target surface (Fig. 6H). The robot can even adhere to a damaged surface with a 10 mm-diameter hole in the middle (Fig. 6I). The robot can also adjust its orientation (90 deg) during swimming and attach it to the sidewall of a water tank. Beyond just attachment, the robot could also grip underwater objects through an air-water transition with a biomimetic disc mounted on its underside. Figure S20 shows the high-speed images of the robot entering the water, grasping a plastic container lid, and pulling the lid out of the water in 4.3 s (Movie S15).

We also investigated the robot's adhesion success rate and adhesion time on a treated surface with an external flow disturbance (a circulating tank flow speed of 0.5 m/s, plus an additional water jet of 3.13 m/s) flowing in the anterior-posterior direction toward the disc (Fig. S21A, Movie S16, Supplementary Text S10). To mimic a slippery surface found in nature, we soaked a surface in a natural lake for two months until various algae grew on the surface (Fig. S21B). The underwater adhesion success rate of the robot was 90% in 22 trials (20 successes and 2 failures). The robot's adhesion time was over 8 hours under this challenging situation (Movie S16). We also quantitatively measured that, under experimental conditions, the robot's oscillations were around 0.74 ± 0.38 mm under a water flow speed of 0.5 m/s in this water tank.

Applications of the aerial-aquatic hitchhiking robot in the wild

Fig. 7A shows the perching ability of the robot in an outdoor environment. The robot can fly and attach to a horizontal roof or the curved and inclined surfaces (with a 45° tilt) of a building (Movie S17). The onboard camera installed on the side of the robot can record videos. For example, we tested the aerial-aquatic transition performance with a waterproof camera in a lake. The robot takes off from land (0 s), flies into the water (3.2 s), and captures underwater video with the camera. Then the robot flies out of the water via a water-to-air transition and captures a broad view of the lake (Fig. 7B, Fig. S22, Movie S18). We show that the robot can fly out of the water and attach to an unstructured, rough rock (Fig. 7C, Fig. S23, Movie S18). We manually attached (i.e., initially attached by hand) the robot to a vertical rock surface in a stream and show that the robot can achieve stable adhesion even on a slippery and uneven surface (Fig. 7D, Fig. S24, Movie S18).

We further tested the robot's performance at natural air-water interfaces. Fig. 8A shows that the robot can take off from the bottom of a flowing stream (time: 3 s) (Movie S19). The onboard camera can record both underwater and aerial images. Fig. 8B shows that the robot could robustly stick to a slippery rock in the flow stream (initially attached by hand). Interestingly, the onboard camera can record videos of the air/water interface with little oscillation, even under the impact of a stream flowing with a speed of ~1.5m/s. Traditional unmanned aerial vehicle (UAV) hovering results in oscillations within a small range of around 1-2 cm (*24*). In contrast, this robot's hitchhiking position was much more stable with only very small oscillations even under flowing water conditions.

The image acquisition ability of the robot is also beneficial to oceanic environmental observation. Fig. 8C shows the robot hitchhiking with a swimming "host" (a remotely operated vehicle moving at a speed of ~1m/s) and obtaining seabed images at a depth of 10-15 m (Fig. S25) and 1-2 m (Fig. 8C) in an operational window of 15 minutes, respectively (Movie S20). Images of marine organisms, including scallops, seaweed, and hermit crabs, were captured by the robot's onboard camera. The robot stays stably attached to the bottom of the vehicle during the entire hitchhiking process. Fig. 8D shows that the robot can also fly up from the seafloor (water depth of about 0.5m, in a duration of 2s), with the onboard camera effectively recording images of both seafloor and coastline (Movie S20). The results also show that the robot can grip an experimental sampling plate with seaweed and take it out of the water via a biomimetic disc on its lower surface (Fig. 8E). Through these outdoor experiments, we show that the robot can hitchhike, record video during air-water transitions, and perform cross-medium retrieval operations in both freshwater and saltwater environments.

DISCUSSION

In this article, we describe an aerial-aquatic hitchhiking robot that is self-contained and remotely controlled for flying, swimming, and attaching to surfaces in both air and water and that can seamlessly move between the two. We primarily overcame two challenges of implementing this robot by creating a robust and adaptable amphibious "hitchhiking" device that could make consecutive transits across the two domains.

The method of biological inspiration follows the Inspire-Abstract-Implement paradigm, whereby the adhesive method of the remora is functionally identified, abstracted, and then implemented on the robotic prototype (*45*). We attribute the exceptional adhesive performance of the "hitchhiking" device to the fundamental principles we derived from the morphological features of the biological remora: redundant, self-adaptive, hydrostatically enhanced adhesion. Based on our experiments, we found that the redundant feature of the biomimetic disc (due to the lamellar compartments) could increase the frictional stress by 44% in air and 15% under water and adhesion time by up to 458% in air and 206% under water. The self-adaptive principle also increased the frictional stress to 61% in air and 30% under water. The hydrostatic enhancement increased the frictional stress up to 56% in air and 41% under water. Furthermore, the disc could attach to curved surfaces and challenging surfaces (narrow, damaged, lumpy, slippery surfaces) that are impossible for a traditional suction-cup attachment. We used a stacked manufacturing approach to incorporate three functional layers in one disc to realize these three adhesive principles (redundant, self-adaptive, hydrostatically enhanced adhesion). We believe that the current manufacturing method can be expanded to include more functional layers, or replace existing layers, to provide the device with additional functionalities to help it adapt to various environments.

This biomimetic disc achieves superior adhesive performance compared to previously described biomimetic discs in terms of adhesion stress, frictional stress, surface adhesive adaptability, and adhesion time. Here we compare the current hitchhiking device with two other biomimetic adhesive devices, the 3D-printed remora-inspired suction cup (*36*) and the clingfish-inspired suction cup (*46*). The maximum adhesion stress of the 3D-printed remora-inspired disc is 58.7 ± 2.2 kPa (tested on a smooth underwater surface) (*36*) and 18.3 ± 0.4 kPa for the clingfish-inspired disc (tested on a rough underwater surface with R_a = 50 μm) (*46*). In contrast, this disc's maximum adhesion stress is 69.6 ± 0.5 kPa (tested on a smooth surface underwater). The maximum frictional stress of the previously

described 3D-printed remora-inspired disc is 4.9 ± 0.1 kPa, although this disc prototype can generate a frictional stress up to 42.9 ± 2.1 kPa. Note that there is no frictional stress data reported for the clingfish-inspired disc. Regarding adhesive adaptability, the maximum surface roughnesses the 3D-printed remora-inspired disc and clingfish-inspired disc can attach to are 200 μm and 269 μm, respectively. In contrast, this disc can attach to a surface with roughness up to R_a = 764 μm with adhesion stress of 38.6 kPa. Another metric for surface adhesive adaptability is the maximum curvature. The 3D-printed remora disc cannot adhere to a curved surface because of its rigid base design (*36*), and the clingfish-inspired disc can attach to a surface with a curvature of u = 1.25. This disc can attach to a surface with a curvature of u = 2.18. In terms of adhesive time, the maximum adhesion time of the clingfish-inspired disc is 383 ± 38 min (wet surface with R_a = 10 μm, σ_l = 3.63 kPa) ($\sigma_l = F_l/A$, where F_l represents the external load acting on the sucker). The current disc has a longer adhesion time of up to 2944.4 ± 143.7 minutes (over 60 h). Thus, the biomimetic disc developed in this work can be regarded as a powerful tool for a hitchhiking robot.

We also compare the water-air transition performance of this robot with that of previously reported robots (see Table S1). The aerial-aquatic robot in this article has several superior qualities: it is untethered, executes rapid transitions (about 0.35 s), maintains excellent stability during transitions (the roll and pitch angles are less than 3 deg), and can execute consecutive transitions (e.g., 7 times in 20.3 seconds). The three existing types of rotor-based aerial-aquatic robots that perform water-to-air transitions either have buoyancy devices (*20, 22*) or apply an additional rotor system (*19*) that reduce the transition speed from water to air.

Previous studies of rotor-based aerial-aquatic robots lack detailed investigations of the air-water transition process (*19*-*22*). Several factors affect transition time, such as the robot's shape, weight, power input of the motors, and more. One important factor for achieving a rapid transition time is shortening the period during which the rotational speed of the propellers rapidly changes at the air-water interface. This allows the robot to rapidly accelerate its propellers from a low rotational speed (underwater) to a high speed (in air) to generate enough force to lift the robot out of the water. We proposed a simple and replicable self-folding propeller design to achieve this. Holding the throttle of the motors constant (50%), the rotational speed of the self-folding propellers changed from 1400 rpm (underwater) to 9600 rpm (in air) within 0.54 ± 0.08 s (Fig. S15). In contrast, the commercial and fixed-unfolded propellers took 1.39 ± 0.16 s and 0.81 ± 0.17 s, respectively, to achieve the speed-changing during the transition. The shortened period for the folding propeller design can be explained by two factors: its resistance underwater is comparatively less, leading to a higher initial rotational speed once it emerges from the water; and at the same motor throttle, the self-folding propeller's ability to accelerate is comparatively greater because it has a smaller diameter when folded, leading to less drag force during the rotatory acceleration. Additional design optimization and fluid analysis of the self-folding propeller design may further enhance the robot's transitional performance.

The aerial-aquatic biomimetic robot can also resist large external longitudinal and tangential forces, thus enabling the robot to “rest” on a stationary surface or “hitchhike” on a moving host to extend its working time and enlarge its monitoring area. Notably, the robot’s hitchhiking state saves power by a factor of 51.7 times (in air) and 19.2 times (under water) compared to remaining in a hovering state.

The limitations of the current robot can be summarized as follows: the biomimetic disc does not include the ability to sense the adhesion and detect its adhesive state. In addition, the current robot can work in water up to a depth of 2.2m with communication. The small onboard underwater wireless communication module limits its work depth and overall working area. Furthermore, the navigation, perception, and autonomous control of the aerial-aquatic robot would complement this prototype in the future. We also envision that the robot can employ machine learning methods for autonomous biological detection, recognition, and tracking in the air-water interface.

MATERIALS AND METHODS

Morphological study of the biological remora disc

To observe the partial adhesion behavior of the live remora (*Echeneis naucrates*), we used a glass rod to guide a live remora to attach to the porous sidewall (hole diameter of 20 mm). Then we captured high-speed videos (FASTCAM Mini UX100, Photron Ltd, Tokyo, Japan) from the lateral view of the remora (Movie S1).

We scanned a preserved remora head obtained from the Museum of Comparative Zoology at Harvard University (MCZ Ichthyology #83209) using microcomputed tomography (Skyscan 1173, Bruker microCT, Kontich, Belgium). Using the reverse modeling software Geomagic (Geomagic Studio, 3D Systems Inc., California, USA), we extracted a single lamella from the 3D reconstructed bony lamella plate and measured the critical morphological angles. The remoras used in this study comply with the regulations for the Administration of Affairs Concerning Experimental Animals issued by the Institutional Animal Care and Use Committee of Beijing.

Fabrication of the biomimetic remora disc

We fabricated the main disc by using a multi-material 3D printer Objet Connex C3 (Stratasys Ltd, Eden Prairie, MN, USA) (Fig. S6B). The main disc's components are 3D printed with different materials. For example, the material of soft lip around the disc base edge and soft tissue of lamellae is TangoPlus FLX930 (Stratasys Ltd, Eden Prairie, MN, USA). The material of rigid lamellae is VeroWhitePlus RGD835 (Stratasys Ltd, Eden Prairie, MN, USA). The flexible base is fabricated by mixed materials of TangoPlus and VeroWhitePlus, RGB 8505 (Stratasys Ltd, Eden Prairie, MN, USA) (Fig. S6B-D). By molding and casting silicone rubber (Ecoflex 10, Smooth-on, Inc, Easton Pa, USA), we fabricated the soft layer (with a thickness of 800 μm) on top of the disc lip (Fig. S6A). The spinules were fabricated by laser-cutting a 200 μm stainless steel plate. Then, the spinules were inserted into the lamellae (Fig. S6D). The lamellae actuator with micro-channels was printed by a multi-material 3D printer using silicone materials (ACEO@ Silicone GP, Wacker Chemie AG, Germany) (Fig. S6E). The bending actuator was fabricated by molding/casting silicone rubber (Mold Star 30, Smooth-on, Inc, Easton Pa, USA) with fiber reinforcements (Fig. S7). Finally, different layers were bonded by silicone rubber adhesive (Sil-Poxy, Smooth-on, Inc, Easton Pa, USA) (Fig. S6F).

Adhesion experiments of the biomimetic discs

We measured the discs' frictional and adhesive stresses on smooth (glass plate) and rough surfaces (sandpaper, 3M, Inc.) using a multiple-axis force transducer (Mini 40 F/T sensor, ATI Technologies Inc., USA) mounted to a robotic arm (MOTOMAN MH3F, YASKAWA Inc., Japan). The moving speed of the robotic arm was set as 1 mm/s. We tested the maximum adhesion time of the prototypes on a rough surface (50 μm) using a mechanical testing machine (Zwick z0.5, Zwick/Roell Co., Ulm, Germany), under loads of 10 N and 30

N. More details of stress and adhesion time measurements can be found in Supplementary S11.

Experiments of the aerial-aquatic robots

In a laboratory water tank (110 × 80 × 70 cm), we tested the transition performance of the robots with the three types of propellers (Fig. 5H, Fig. S15). A high-speed camera (FASTCAM Mini UX100, Photron Ltd, Tokyo, Japan) recorded the transition processes on the tank's side for calculating the transition time. The transition trajectories were recorded by the high-speed camera (sampling rate: 250 frames per second) and then reconstructed in MATLAB R2020a (MathWorks, MA, USA). The robot's flight controller (Ominibus F4v3 Flight Controller, Airbot, Shenzhen, China) recorded the rotational speeds, the roll angle, and the pitch angle during the robot's medium transition.

For the experimental setup of robot hitchhiking, we controlled the robot to move vertically up to attach a smooth acrylic board installed on a moving guide rail. The guide rail was programmed to move at controlled speeds (0.1, 0.3, and 0.5 m/s). The experiments were conducted in a water tank of 7.8 meters in length, 1.2 meters in width, and 1.1 meters in height. A six-axis force sensor (Delta, ATI industrial, Inc., USA) and a high-speed camera were fixed above the acrylic board to collect force data and the high-speed videos.

Statistical analyses

We used one-way (Fig. 4B, 4I) and two-way (Fig. 4E, 4G, 4H, Fig. 5I) analyses of variance (ANOVA) to evaluate the significant difference in the experimental results. Error bars and error bands represent ± 1 SD. The level of statistical significance was set at $P < 0.05$. All statistical analyses were conducted in OriginPro Version 2018 (OriginLab, USA).

Supplementary Materials

Movie S16. Adhesion success rate and adhesion time of the robot in flowing water.
Movie S17. Robot perching on buildings in the air.
Movie S18. Robotic performance in a lake.
Movie S19. Robotic performance in a natural flowing stream.
Movie S20. Robotic performance in the ocean.

References and Notes

1. G. Li, X. Chen, F. Zhou, Y. Liang, Y. Xiao, X. Cao, Z. Zhang, M. Zhang, B. Wu, S. Yin, Self-powered soft robot in the Mariana Trench. *Nature*. **591**, 66-71 (2021).
2. K. C. Galloway, K. P. Becker, B. Phillips, J. Kirby, S. Licht, D. Tchernov, R. J. Wood, D. F. Gruber, Soft robotic grippers for biological sampling on deep reefs. *Soft Robot*. **3**, 23-33 (2016).
3. G. Brantner, O. Khatib, Controlling Ocean One: Human-robot collaboration for deep-sea manipulation. *J. Field Robot.* **38**, 28-51 (2021).
4. H. Jiang, E. W. Hawkes, C. Fuller, M. A. Estrada, S. A. Suresh, N. Abcouwer, A. K. Han, S. Wang, C. J. Ploch, A. Parness, M. R. Cutkosky, A robotic device using gecko-inspired adhesives can grasp and manipulate large objects in microgravity. *Sci. Robot.* **2**, eaan4545 (2017).
5. N. D. Naclerio, A. Karsai, M. Murray-Cooper, Y. Ozkan-Aydin, E. Aydin, D. Goldman, E. W. Hawkes, Controlling subterranean forces enables a fast, steerable, burrowing soft robot. *Sci. Robot.* **6**, eabe2922 (2021).
6. M. Hassanalian, A. Abdelkefi, Classifications, applications, and design challenges of drones: A review. *Prog. Aerosp. Sci.* **91**, 99–131 (2017).
7. F. E. Fish, Advantages of aquatic animals as models for bio-inspired drones over present AUV technology. *Bioinspir. Biomim.* **15**, 025001 (2020),
8. R. Salazar, V. Fuentes, A. Abdelkefi, Classification of biological and bioinspired aquatic systems: A review. *Ocean Eng.* **148**, 75–114 (2018).
9. R. R. Murphy, E. Steimle, C. Griffin, C. Cullins, M. Hall, K. Pratt, Cooperative use of unmanned sea surface and micro aerial vehicles at Hurricane Wilma. *J. Field Robot.* **25**, 164-180 (2008).
10. K. H. Low, T. Hu, S. Mohammed, J. Tangorra, M. Kovac, Perspectives on biologically inspired hybrid and multi-modal locomotion. *Bioinspir. Biomim.* **10**, 020301 (2015).
11. S. Zimmerman, A. Abdelkefi, Review of marine animals and bioinspired robotic vehicles: Classifications and characteristics. *Prog. Aerosp. Sci.* **93**, 95–119 (2017).
12. R. Siddall, M. Kovač, Launching the AquaMAV: Bioinspired design for aerial–aquatic robotic platforms. *Bioinspir. Biomim.* **9**, 020301 (2014).
13. W. Weisler, W. Stewart, M. B. Anderson, K. J. Peters, A. Gopalarathnam, M. Bryant, Testing and characterization of a fixed wing cross-domain unmanned vehicle operating in aerial and underwater environments. *IEEE J. Ocean. Eng.* **43**, 969-982 (2017).
14. D. Caruccio, M. Rush, P. Smith, J. Carroll, P. Warwick, E. Smith, C. Fischer, K. Motylinski, L. F. Vasconcelos, P. Costa et al., Design, fabrication, and testing of the fixed-wing air and underwater drone, in *17th AIAA Aviation Technology, Integration, and Operations Conference* (2017), pp. 4447.
15. R. Zufferey, A. O. Ancel, A. Farinha, R. Siddall, S. F. Armanini, M. Nasr, R. V. Brahmal, G. Kennedy, M. Kovac, Consecutive aquatic jump-gliding with water-reactive fuel. *Sci. Robot.* **4**, eaax7330 (2019).
16. R. Siddall and M. Kovac, Fast aquatic escape with a jet thruster. *IEEE-ASME Trans. Mechatron.* **22**, 217-226 (2017).
17. T. Hou, X. Yang, H. Su, B. Jiang, L. Chen, T. Wang, J. Liang, Design and experiments of a squid-like aquatic-aerial vehicle with soft morphing fins and arms, in *2019 International Conference on Robotics and Automation* (2019), pp. 4681-4687.
18. Y. Chen, H. Wang, E. F. Helbling, N. T. Jafferis, R. Zufferey, A. Ong, K. Ma, N. Gravish, P. Chirarattananon, M. Kovac, A biologically inspired, flapping-wing, hybrid aerial-aquatic microrobot. *Sci. Robot.* **2,** eaao5619 (2017).

19. M. M. Maia, D. A. Mercado and F. J. Diez, Design and implementation of multirotor aerial-underwater vehicles with experimental results, in *2017 IEEE/RSJ International Conference on Intelligent Robots and Systems* (2017), pp. 961-966.
20. H. Alzu'bi, I. Mansour, O. Rawashdeh, Loon copter: Implementation of a hybrid unmanned aquatic-aerial quadcopter with active buoyancy control. *J. Field Robot.* **35**, 764-778 (2018).
21. Zha, J., Thacher, E., Kroeger, J., Mäkiharju, S. A., & Mueller, M. W, Towards breaching a still water surface with a miniature unmanned aerial underwater vehicle, in *2019 International Conference on Unmanned Aircraft Systems* (2019), pp. 1178-1185.
22. D. Lu, C. Xion, Z. Zeng, L. Lian, A multimodal aerial underwater vehicle with extended endurance and capabilities, in *2019 International Conference on Robotics and Automation* (2019), pp. 4674-4680.
23. M. A. Graule, P. Chirarattananon, S. B. Fuller, N. T. Jafferis, K. Y. Ma, M. Spenko, R. Kornbluh, R. J. Wood, Perching and takeoff of a robotic insect on overhangs using switchable electrostatic adhesion. *Science*. **352**, 978-982 (2016).
24. K. Hang, X. Lyu, H. Song, J.A. Stork, A. M. Dollar, D. Kragic, F. Zhang, Perching and resting-A paradigm for UAV maneuvering with modularized landing gears. *Sci. Robot.* **4,** eaau6637 (2019).
25. K. M. Popek, M. S. Johannes, K. C. Wolfe, R. A. Hegeman, R. J. Bamberger, Autonomous grasping robotic aerial system for perching (AGRASP), in *2018 IEEE/RSJ International Conference on Intelligent Robots and Systems* (2018), pp. 1-9.
26. C. E. Doyle, J. J. Bird, T. A. Isom, J. C. Kallman, D. F. Bareiss, D. J. Dunlop, R. J. King, J. J. Abbott, M. A. Minor, An avian-inspired passive mechanism for quadrotor perching. *IEEE-ASME Trans. Mechatron.* **18**, 506-517 (2012).
27. L. Daler, A. Klaptocz, A. Briod, M. Sitti, D. Floreano, A perching mechanism for flying robots using a fibre-based adhesive, in *2013 IEEE International Conference on Robotics and Automation* (2013), pp. 4433-4438.
28. S. Liu, W. Dong, Z. Ma, X. Sheng, Adaptive Aerial Grasping and Perching with Dual Elasticity Combined Suction Cup. *IEEE Robot. Autom. Lett.* **5**, 4766-4773 (2020).
29. H. N. Nguyen, R. Siddall, B. Stephens, A. Navarro-Rubio, M. Kova, A passively adaptive microspine grapple for robust, controllable perching, in *2019 2nd IEEE International Conference on Soft Robotics* (2019), pp. 80-87.
30. M. T. Pope, C. W. Kimes, H. Jiang, E. W. Hawkes, M. A. Estrada, C. F. Kerst, W. R. T. Roderick, A. K. Han, D. L. Christensen, M. R. Cutkosky, A multimodal robot for perching and climbing on vertical outdoor surfaces. *IEEE Trans. Robot.* **33**, 38-48 (2016).
31. J. F. Roberts, J. C. Zufferey, D. Floreano, Energy management for indoor hovering robots, in *2008 IEEE/RSJ International Conference on Intelligent Robots and Systems* (2008), pp. 1242-1247.
32. Y. Chen, M. C. Shih, M. H. Wu, E. C. Yang, K. J. Chi, Underwater attachment using hairs: the functioning of spatula and sucker setae from male diving beetles. *J. R. Soc. Interface*. **11**, 20140273 (2014).
33. H. L. Schoenfuss, R. W. Blob, Kinematics of waterfall climbing in hawaiian freshwater fishes (Gobiidae): vertical propulsion at the aquatic terrestrial interface. *J. Zool.* **261**, 191-205 (2003).
34. F. Andreas, Walking on Suckers: New insights into the locomotory behavior of larval net-winged midges (Diptera: Blephariceridae). *J. N. Am. Benthol. Soc.* **17**, 104-120 (1998).
35. D. Weihs, F. E. Fish, A. J. Nicastro, Mechanics of remora removal by dolphin spinning. *Mar. Mamm. Sci.* **23**, 707-714 (2007).

36. Y. Wang, X. Yang, Y. Chen, D. K. Wainwright, C. P. Kenaley, Z. Gong, Z. Liu, H. Liu, J. Guan, T. Wang, A biorobotic adhesive disc for underwater hitchhiking inspired by the remora suckerfish. *Sci. Robot.* **2**, eaan8072 (2017).
37. K. M. Gamel, A. M. Garner, B. E. Flammang, Bioinspired remora adhesive disc offers insight into evolution. *Bioinspir. Biomim.* **14**, 056014 (2019).
38. S. Wang, L. Li, W. Sun, D. Wainwright, H. Wang, W. Zhao, B. Chen, Y. Chen, L. Wen, Detachment of the remora suckerfish disc: kinematics and a bio-inspired robotic model. *Bioinspir. Biomim.* **15**, 056018 (2020).
39. K. E. Cohen, C. H. Crawford, L. P. Hernandez, M. Beckert, B. E. Flammang, Sucker with a fat lip: The soft tissues underlying the viscoelastic grip of remora adhesion. *J. Anat.* **237**, 643-654 (2020).
40. S. Su, S. Wang, L. Li, L. Li, Z. Xie, F. Hao, J. Xu, S Wang, J. Guan, L. Wen, Vertical Fibrous Morphology and Structure-Function Relationship in Natural and Biomimetic Suction-Based Adhesion Discs. *Matter*. **2**, (2020).
41. K. E. Cohen, B. E. Flammang, C. H. Crawford, L. P. Hernandez, Knowing when to stick: touch receptors found in the remora adhesive disc. *R. Soc. Open Sci.* **7**, 190990 (2020).
42. B. E. Flammang, C. P. Kenaley, Remora cranial vein morphology and its functional implications for attachment. *Sci Rep*. **7**, 1-5 (2017).
43. K. Autumn, Y. A. Liang, S. T. Hsieh, W. Zesch, W. P. Chan, T. W. Kenny, R. Fearing, R. J. Full, Adhesive force of a single gecko foot-hair. *Nature*. **405**, 681-685 (2000).
44. D. M. Drotlef, L. Stepien, M. Kappl, W. J. P. Barnes, H. J. Butt, A. del Campo, Insights into the adhesive mechanisms of tree frogs using artificial mimics. *Adv. Funct. Mater.* **23**, 1137-1146 (2013).
45. M. Kovac, The bioinspiration design paradigm: A perspective for soft robotics. *Soft Robot*. **1**, 28-37 (2014).
46. J. A. Sandoval, S. Jadhav, H. Quan, D.D. Deheyn, M.T. Tolley, Reversible adhesion to rough surfaces both in and out of water, inspired by the clingfish suction disc. *Bioinspir. Biomim.* **14**, 066016 (2019).

Acknowledgments: We thank Zemin Liu, Dongjun Wang, Yanru Mo, Wenbo Liu and Zhaoning Sun for their contribution to this work, and Dylan Wainwright for providing Micro CT data of the remora head.

Funding: This work was supported by:
National Science Foundation of China grant Nos. 91848105,
91848206, 92048302, 61633004, 61822303, T2121003.
National Key R&D Program of China grant Nos. 18YFB1304600, 2019YFB1309600, 2020YFB1313003.
Academic Excellence Foundation of BUAA for Ph.D. Students (to LL)
EPSRC, and the EU H2020 AeroTwin project (to MK)
Royal Society Wolfson fellowship grant No. RSWF/R1/18003 (to MK)

Author contributions: LL, SQW, and LW conceived the project. LL, SQW, BHC, and LW designed and fabricated the biomimetic remora disc. LL, SQW, and LW characterized the morphology of the biological remora disc. LL, FQY, WZ and LW conducted the adhesive experiments and analyzed the data. LL, SYS, SQW, SCT and LW integrated the aerial-aquatic robotic system. LL, SYS, YYZ, WGS, GW, JQL, and LW conducted the

experiments on the robotic system and analyzed the data. LL, SQW, YYZ, PN, MK, and LW prepared the manuscript. All authors provided feedback during subsequent revisions.

Competing interests: Authors declare that they have no competing interests.

Data and materials availability: All data are available in the main text or the supplementary materials.

Figures:

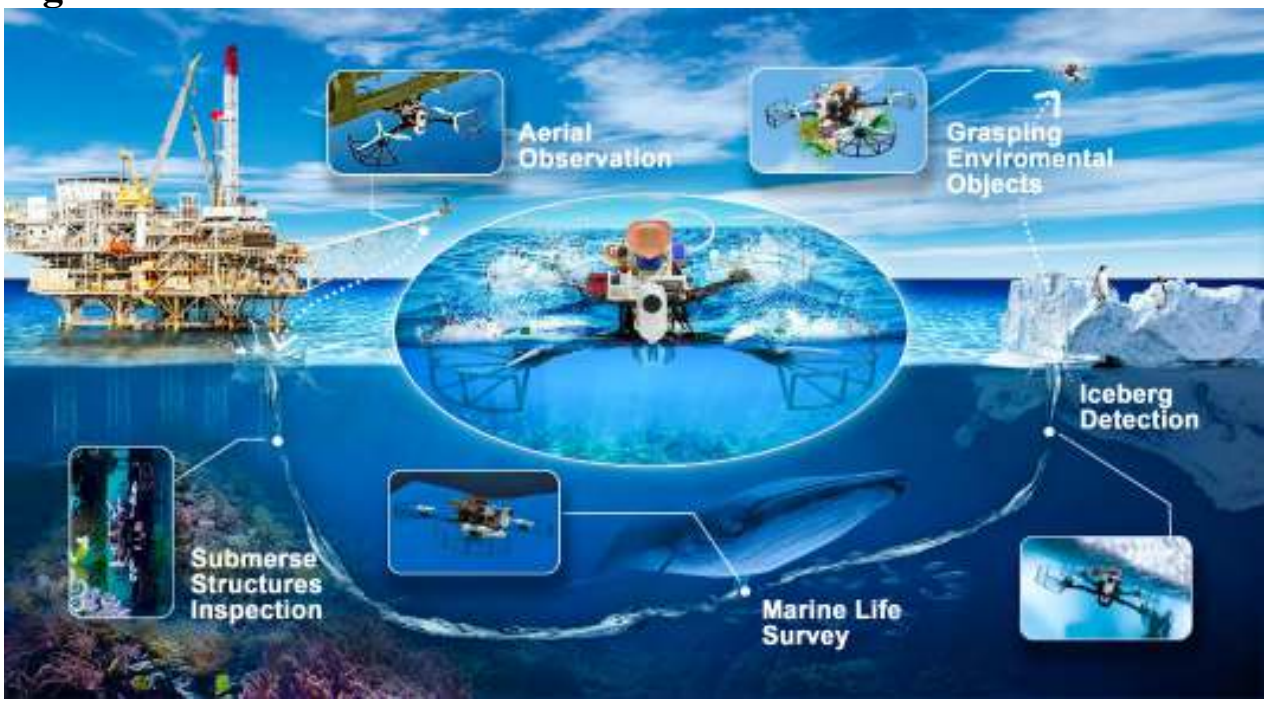

Fig. 1. A depiction of the mission profile and design of an aerial-aquatic hitchhiking robot. The robot's ability to transition across water and air and attach robustly to a wide variety of surfaces allows it to perform long-term missions (such as monitoring) in natural environments. All image elements from the third party are approved with licenses.

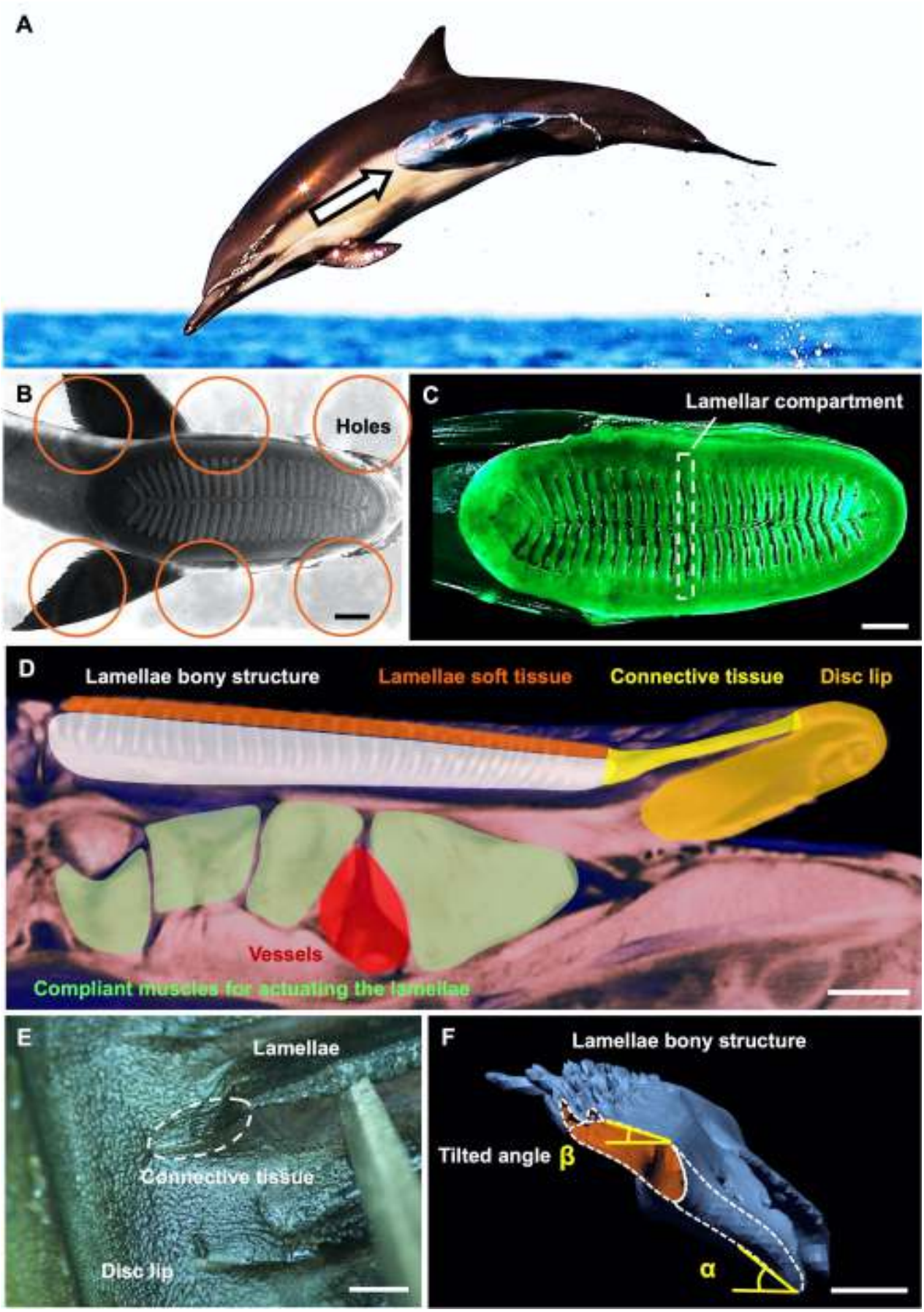

Fig. 2. Morphological features of the remora's adhesive structures. (A) Remoras can remain attached in the air: a remora stays firmly attached to the side of a dolphin as it leaps through the

air in an attempt to dislodge parasites (photo credit: Maxence Atzori). **(B)** Remoras can attach to a porous surface on the side of an aquarium (scale bar is 1 cm, Movie S1). **(C)** FTIR image (dorsal view) of an anesthetized remora attaching to transparent glass in the air. The green fluorescent area indicates where the disc is in contact with the glass substrate; the dark black area indicates the disc's lamellar compartments, which are not in contact with the surface (scale bar is 1 cm, Movie S2). **(D)** Cross-sectional view of the micro-CT scan of a remora head and disc pad laying on its dorsal side (scale bar is 2 mm). **(E)** The thin layer of connective tissue, which seamlessly joins the lamellae and the peripheral disc lip, shown with a light microscope (scale bar is 4 mm, Movie S3). **(F)** Three-dimensional reconstructed model of a single lamella's bony structure from the lateral view. The oblique angle between the lamellae ventral process and the attachment surface (α) and the angle between the lamella's top surface and the attachment surface (β) are shown. The angles (α and β) are averages from all the lamellae of a remora (scale bar is 2 mm).

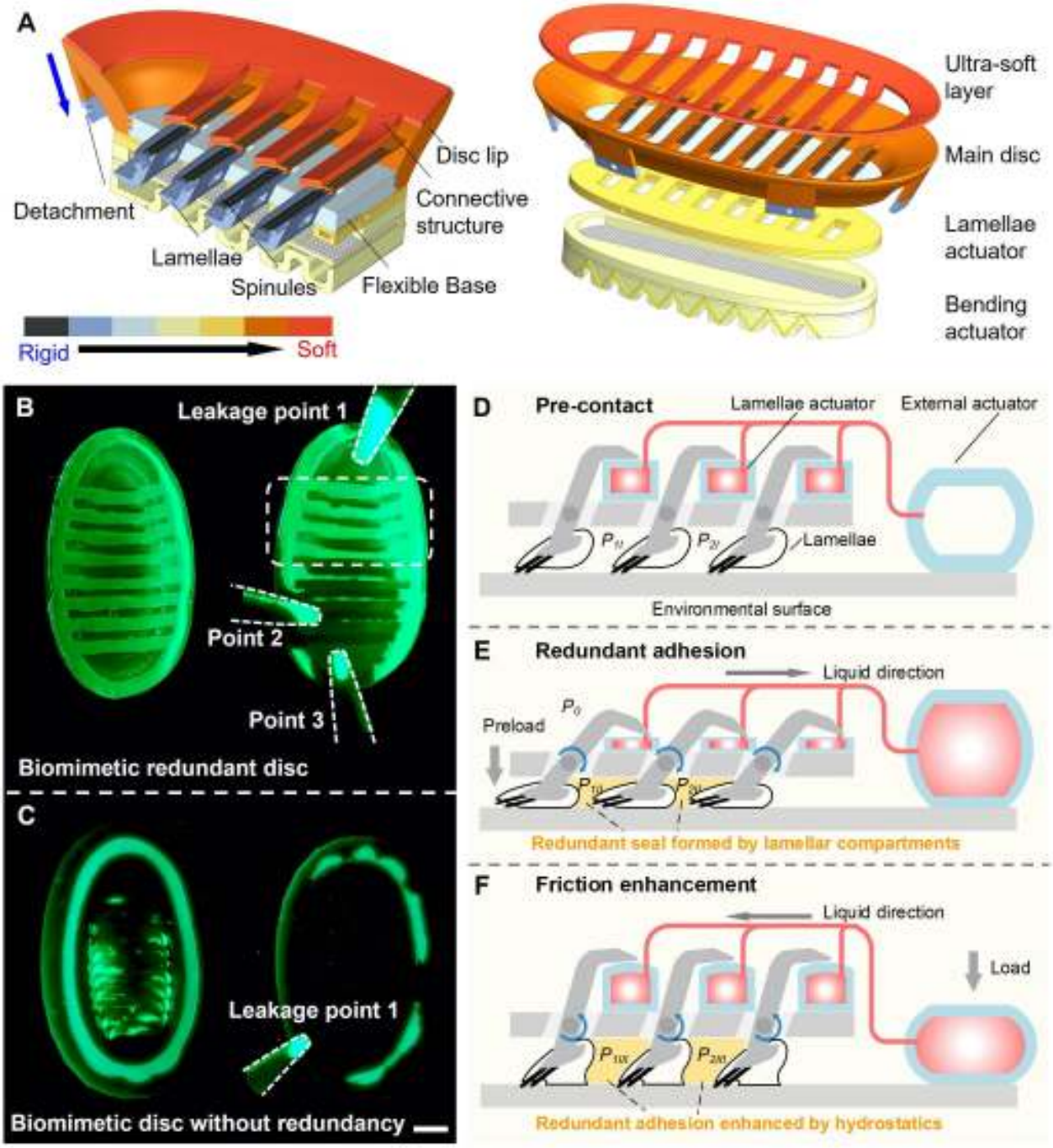

Fig. 3. The implementation and working principle of the redundant biomimetic adhesive disc. **(A)** CAD model of the biomimetic remora disc prototype (disc length, 87 mm; width, 46 mm). Cross-sectional images of the biomimetic prototype show the lamellae, connective structure, disc lip, flexible base, and soft actuator. The disc consists of four functional layers: a thin ultra-soft layer to connect the lamellae and disc lip; a multi-material 3D-printed main disc; a thin fluidic actuated microchannel network layer for rotating the lamellae; and a soft fluidic actuator strengthened by fibers for bending the disc. Different colors indicate materials with different mechanical stiffnesses. **(B-C)** Contact surfaces of the redundant and non-redundant biomimetic adhesive discs (FTIR images). The green color indicates the contact area of the discs on a smooth, transparent substrate. The scale bar is 10 mm. **(B)** Left: the redundant disc formed nine lamellar compartments during attachment. Right: after breaking the seal from three positions, the redundant disc remains attached

using the rest of its compartmentalized chambers. **(C)** Left: the non-redundant disc formed one single chamber throughout the disc lip. Right: the non-redundant disc immediately detached after creating one leakage point (Movie S4). Three stages of the disc adhesion process are summarized in (D)-(F). **(D)** Pre-contact (Stage one). **(E)** Self-adaptive, redundant adhesion (Stage two). **(F)** Frictional enhancement by hydrostatic force (Stage three). The internal pressures of the two compartment chambers are denoted P_1 and P_2, respectively. P_0 represents the fluid pressure of the environment.

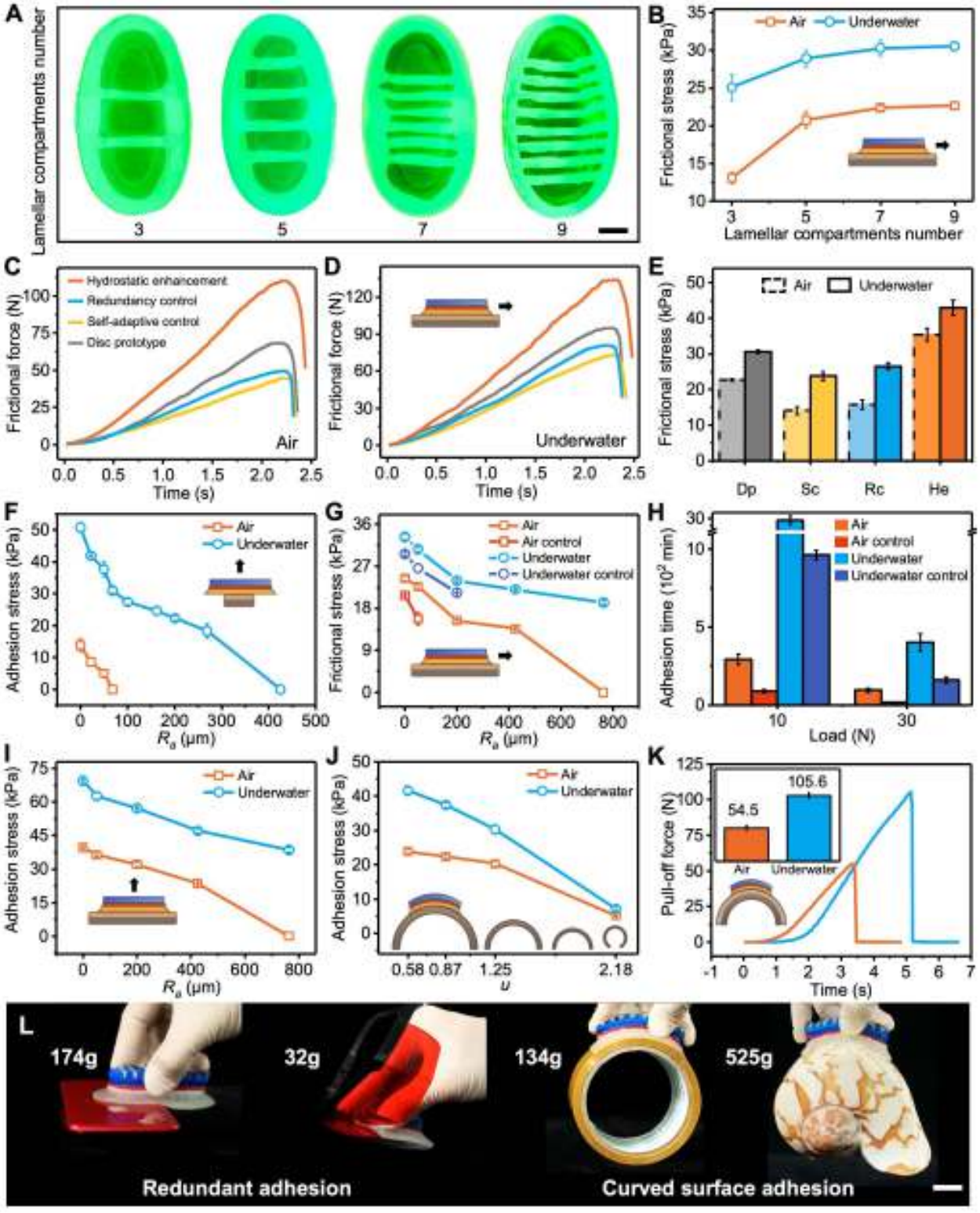

Fig. 4. The adhesive performance of the biomimetic disc both in air and under water. **(A)** Contact surface measurements of adhesive discs with 2, 4, 6, and 8 rows of lamellae (FTIR images). The green color indicates the contact area of the discs on a smooth, transparent substrate. The scale bar is 10 mm. **(B)** The frictional stress of disc prototypes on a rough surface (surface roughness: 50 μm) in air and under water ($N = 5$). **(C)** The static frictional force results (along the horizontal shear direction) of the disc prototypes in air. The following four scenarios were compared: the fully functional biomimetic disc with hydrostatic enhancement; disc control without lamellae compliance; disc control without lamellae compartments; disc with lamellae

compartments and compliance, but without hydrostatic enhancement. **(D)** The static frictional force results (along the horizontal shear direction) of the disc prototypes under water. **(E)** Corresponding maximum static frictional stress on the rough surface (R_a = 50 μm) in air and water (N = 5) (frictional stress = frictional force/disc area). **(F)** The maximum adhesion stress of the disc with only three lamellar compartments (the mid-portion of the disc) attached to surfaces of different roughnesses both in air and under water (N = 5) (Adhesion stress = adhesion force/ disc area). **(G)** The frictional stress of the disc prototypes (with and without lamellar compartments) on different rough surfaces in air and under water (N = 5). **(H)** Comparison of the adhesion time of the disc prototypes with and without lamellar compartments in air and under water (under preloads of 10 N and 30N, respectively) (N = 3). **(I)** The pull-off adhesion stress (along the vertical direction) of the disc on surfaces with different surface roughnesses (from 0 μm to 764 μm) both in air and under water (N = 5). **(J)** The pull-off adhesion stress of the disc prototype on curved surfaces both in air and under water (N = 5). **(K)** The disc's representative force-time profiles on a rough, curved surface (R_a = 50 μm, u = 0.87) both in air and under water. **(L)** The biomimetic disc's redundant adhesion enabled grasping various objects with different sizes, surface curvature, and weights. The scale bar is 2 cm. All error bars represent ± 1 SD.

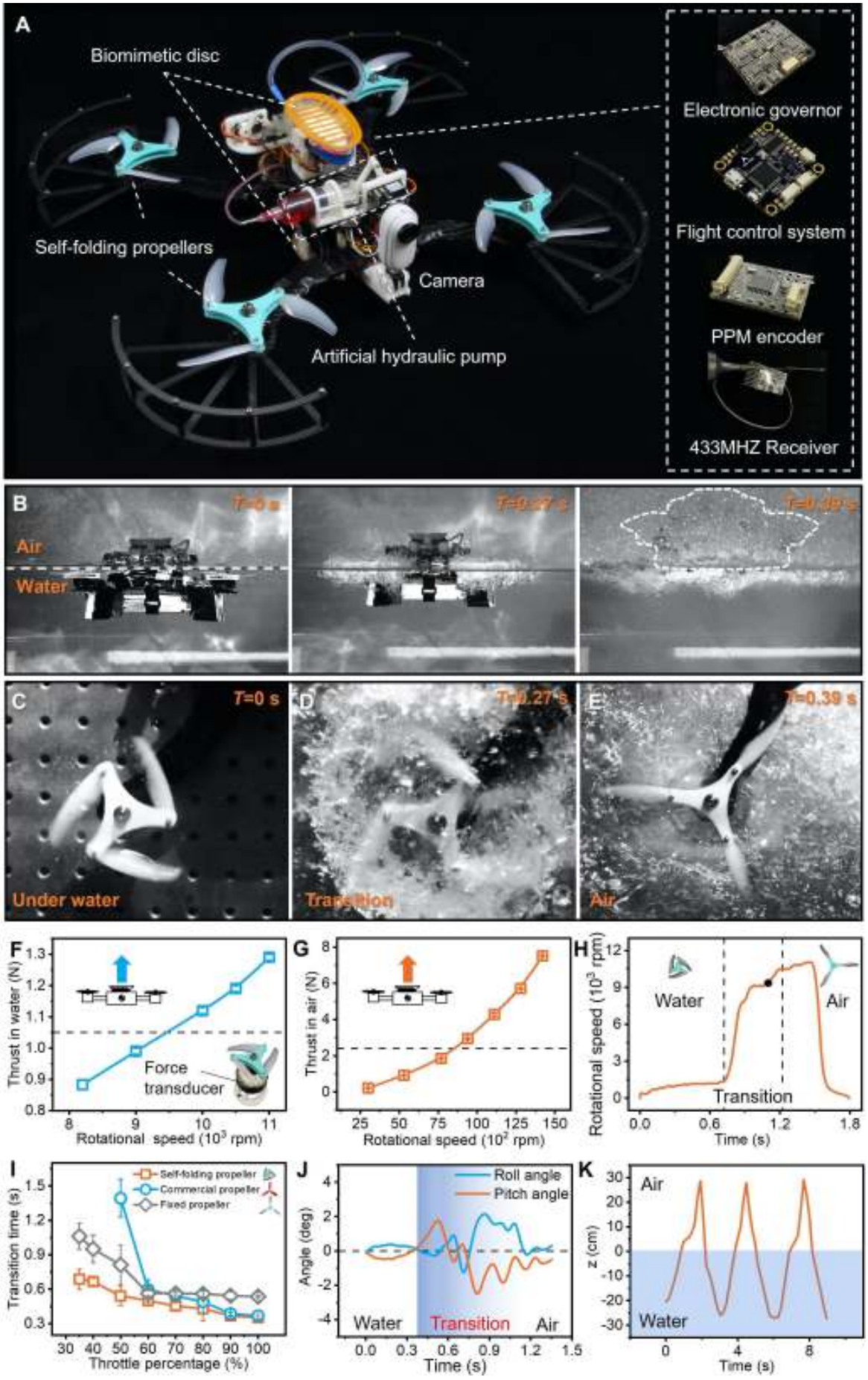
A
Biomimetic disc
Self-folding propellers
Camera
Artificial hydraulic pump
Electronic governor
Flight control system
PPM encoder
433MHZ Receiver
B
Air
Water
C
T=0 s
Under water
D
Transition
E
Air
F
Thrust in water (N)
Force transducer
Rotational speed (10^3 rpm)
G
Thrust in air (N)
Rotational speed (10^3 rpm)
H
Rotational speed (10^3 rpm)
Water
Air
Transition
Time (s)
I
Self-folding propeller
Commercial propeller
Fixed propeller
Transition time (s)
Throttle percentage (%)
J
Roll angle
Pitch angle
Angle (deg)
Water
Transition
Air
Time (s)
K
Air
z (cm)
Water
Time (s)

Fig. 5. Aerial-aquatic hitchhiking robot with self-folding propellers and its air/water transition performance. This robot is self-contained; it can be remotely controlled for flying, swimming, and attaching to surfaces in air and water, and it transits across the two media. **(A)** A top view of the untethered robot and its main components. **(B)** Images of the robot taking off from water at various time instants in a laboratory water tank. **(C-E)** Self-folding propeller performance during the water to air transition. **(C)** The propeller remains folded underwater while rotating. **(D)** A high-speed image of the propeller extending on its own at the water-air interface. **(E)** The propeller fully unfolds in the air. **(F-G)** Thrust force of the self-folded propeller at different rotational speeds under water **(F)** and in the air **(G)** ($N = 5$). The critical rotational speeds (and corresponding forces) are marked by dashed horizontal lines in **(F)** and **(G)**. By exceeding the critical rotational speeds (actuated by the same throttle percentage of motor), the robot can move upward underwater (blue dashed line in panel **F**) or fly up in air (red dashed line in panel **G**). **(H)** The propeller's rotational speed (averaged across all four rotors) as a function of time during the transition from water to air. The area between the two black dashed lines represents the transition process, which started from when the robot's propellers touched the water surface and ended when the robot was entirely out of the water. The black dot indicates when the self-folding propeller achieved the necessary rotational speed to lift the robot up (8500 rpm). **(I)** Comparison of the transition time of the self-folding propeller, commercial propeller, and self-folding propeller fixed in an unfolded state across different throttle percentages ($N = 5$). **(J)** The roll and pitch angles of the robot vs. time during one typical water-to-air transition. **(K)** Three typical cycles of the robot continuously transiting the air-water boundary (Movie S10). All error bars represent ± 1 SD.

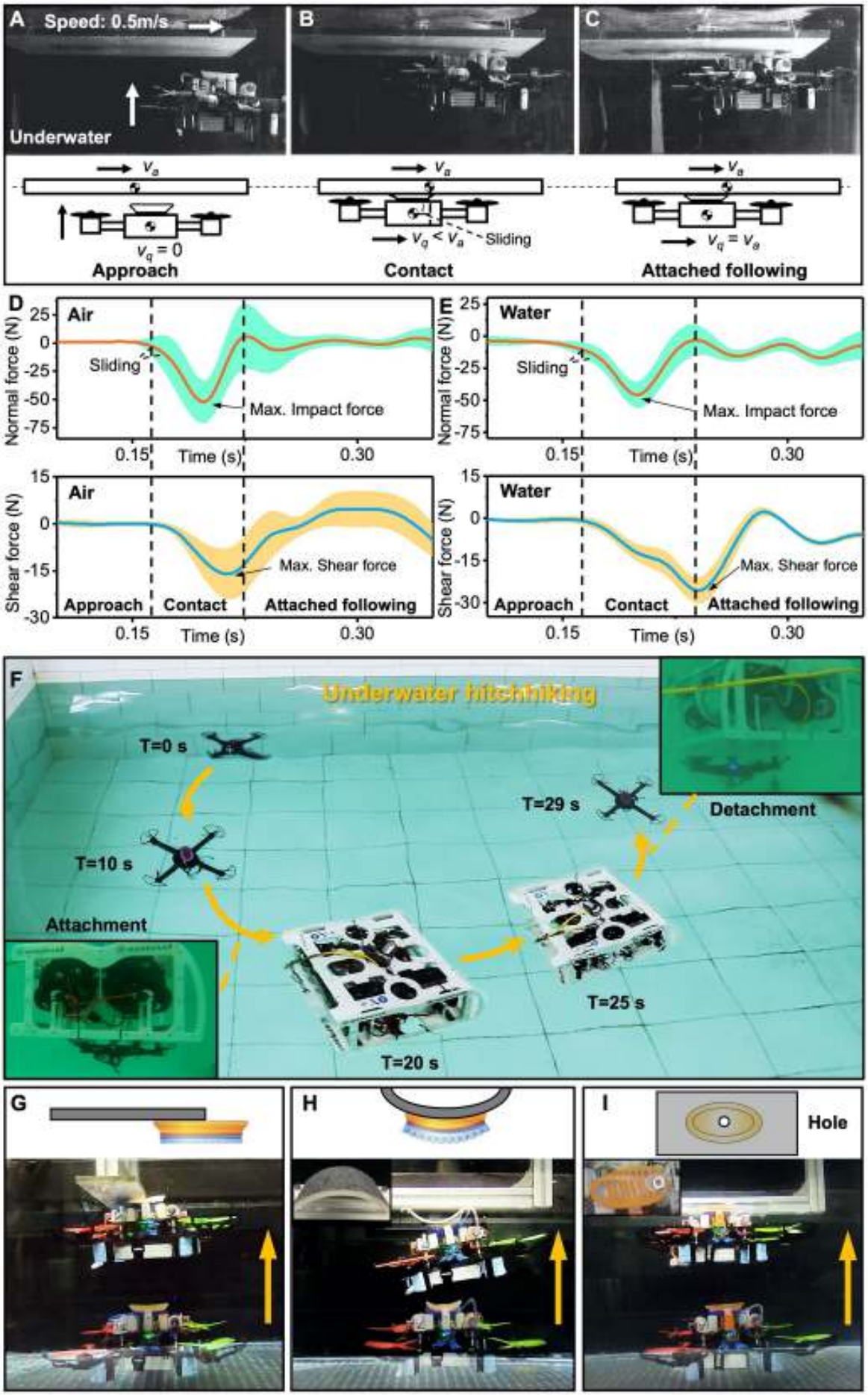
A
Speed: 0.5m/s
Underwater
B
C
v_a
$v_q = 0$
Approach
$v_q < v_a$
Sliding
Contact
$v_q = v_a$
Attached following
D
Air
Sliding
Max. Impact force
Normal force (N)
Time (s)
E
Water
Shear force (N)
Max. Shear force
Approach
Contact
Attached following
F
Underwater hitchhiking
T=0 s
T=10 s
Attachment
T=20 s
T=25 s
T=29 s
Detachment
G
H
I
Hole

Fig. 6. Hitchhiking onto a moving object and adhesive performance of the aerial-aquatic robot. (A-C) High-speed images of the robot hitchhiking onto a moving plate (smooth acrylic) under water. The plate moves from the left to the right at controlled speeds. The robot moves vertically upward until it attaches to the plate. The hitchhiking process was divided into three stages. A video of hitchhiking onto the moving surface is available in **Movie S13**. **(A)** the approach stage, **(B)** the contact stage, and **(C)** the attached-following stage. Note that the high-speed camera was mounted on the moving carriage and has the same speed and direction as the plate. The plate's vertical and shear forces were measured as the robot hitchhiked through the air **(D)** and under water **(E)** as the plate moved at a speed of 0.5 m/s (N = 3). Shaded error bars represent ± 1 SD. Curves were fitted by B-splines. **(F)** The robot demonstrating hitchhiking behavior in a laboratory pool (see Movie S13). The inset images were taken underwater and showed the robot's attachment and detachment to the "host" (a remotely operated vehicle). **(G-I)** Demonstrating the robot's redundant adhesion ability. **(G)** The robot can attach to the narrow acrylic surface with only half of its disc. **(H)** The robot can also adhere to a curved, rough surface and a damaged surface with a 10 mm-diameter hole in the middle **(I)**.

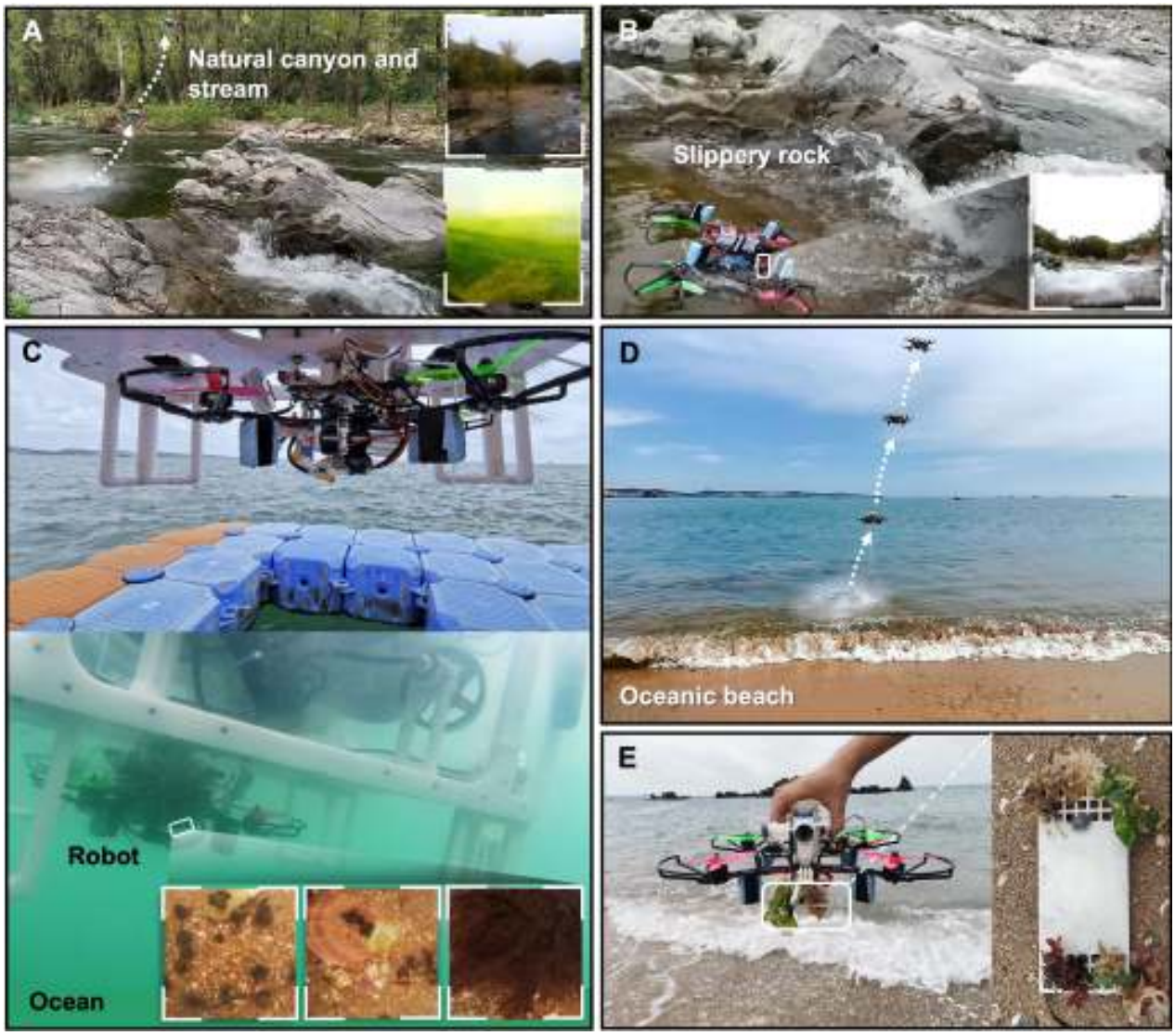

Fig. 8. Performance of the aerial-aquatic hitchhiking robot in the wild. (A) The robot taking off from a flowing freshwater stream (Movie S19). The two image panels on the right show the aerial (upper) and underwater (lower) images from the onboard camera. **(B)** After being initially attached by hand, the robot is capable of robustly remaining attached to a slippery rock in a natural stream flowing with a speed of ~1.5m/s (Movie S19). The image panel on the right shows an onboard camera image with only small oscillation. **(C)** The robot attaching to the bottom of a swimming "host" (a remotely operated vehicle). Images of the seabed at the right include scallops, seaweed, a soldier crab, and more (Movie S20). **(D)** The robot flew out of the seawater of an oceanic beach (Movie S20). **(E)** With a biomimetic disc positioned underneath, the robot gripped a flat sample plate with seaweed and removed it from the water (Movie S20).

Supplementary materials

Title: Aerial-aquatic robots capable of crossing the air-water boundary and hitchhiking onto surfaces

Authors:

Lei Li,[1]† Siqi Wang,[1]† Yiyuan Zhang,[2]† Shanyuan Song,[1] Chuqian Wang,[1] Shaochang Tan,[3] Wei Zhao,[1] Gang Wang,[1] Wenguang Sun,[1] Fuqiang Yang,[1] Jiaqi Liu,[1] Bohan Chen,[1] Haoyuan Xu,[1] Pham Nguyen,[4] Mirko Kovac,[4,5] Li Wen[1]*

Affiliations:

[1]School of Mechanical Engineering and Automation, Beihang University, China.
[2]School of General Engineering, Beihang University, China.
[3]School of Automation Science and Electrical Engineering, Beihang University, China.
[4]Imperial College London, London, UK.
[5]Materials and Technology Centre of Robotics, Swiss Federal Laboratories for Materials Science and Technology (Empa), Switzerland.

*Corresponding author. Email: liwen@buaa.edu.cn
† These authors contributed equally to this work.

This file includes:

Texts S1 to S11
Tables S1 to S2
Figs. S1 to S25

Supplementary Text S1. Mechanical model of redundant adhesive disc

The adhesion force of the bioinspired redundant adhesive disc (Fig. S8) can be represented in the following equation. This model will be experimentally validated in future work.

$$F_a = P_0\left[A - \sum_{k=1}^{n+1} x_k A_k\right] - \sum_{k=1}^{n+1}\left[1 - x_k\right] P_k A_k - F_e + F_b \quad (1)$$

where F_a represents the adhesion force of the disc, P_0 represents the ambient pressure, A represents the area of the disc pad, P_k represents the internal pressure of the lamellar compartment, A_k represents the area of the lamellar compartment, n represents the number of lamellae in the disc, and F_e represents the external load. F_b represents the resultant force of gravity and (negligible) buoyancy of the disc. x_k represents the state of k^{th} lamellar compartment. When the k^{th} compartment is broken, $x_k = 1$. When the k^{th} compartment remains sealed, $x_k = 0$.

Supplementary Text S2. A mechanical model of lamellae

The flexible lamellae of a suction disc can be passively rotated, and the resulting tilt angle facilitates the formation of independent adhesion compartments. These compartments can be achieved even in the presence of lamellae spinules. The flexible passive rotation of the lamellae and the tilt angle eliminate the negative impact of spinules on adhesion ability without affecting the friction-enhancing function of the spinules.

The biomechanical model of lamellae rotation under an external load is actually quite simple, as shown in Fig. S9B,

where the relationship between α and β is:

$$\beta_0 - \beta = \alpha_0 - \alpha \quad (2)$$

The relationship between preload force F_P and lamellae force F_{La} is:

$$F_P L_1 \cos\beta = F_{La} L_2 \quad (3)$$

The deformation displacement of the lamellae is as follows:

$$\triangle h = L_1(\sin\beta_0 - \sin\beta) \quad (4)$$

When lamellae are passively rotated under an external load (F_P), the ventral process interacts with the soft material, which causes the lamellae angle (β) to change to 0 degrees and attach to the substrate to achieve a redundant adhesive state. Then, the active force F_{La} actuates the lamellae to erect up to enhance the frictional force of the attachment. In the current study, the lamellae angle β (18°) and lamellae shape were determined based on the CT model of the biological remora.

Supplementary Text S3. Adhesion performance of the biomimetic disc

We found that passively rotatable lamellae with an angled top surface were vital for the self-adaptive adhesion of the disc (Figs. S9C and S9D). Compared to the lamellae without passive rotation (blue, $\alpha = 90°$, $\beta = 18°$) and a flat top (yellow, $\alpha = 70°$, $\beta = 0°$), the passively rotatable lamellae with an angled top surface (red, $\alpha = 70°$, $\beta = 18°$) generated a notably larger pressure differential between the inside and outside of the lamellar compartment during attachment (Figs. S9C and S9D).

We investigated the effect of using materials with different moduli to fabricate the ultra-soft (connective) layer (Ecoflex 10~55 kPa, Dragonskin 20~300 kPa, and MoldStar 30~600 kPa) on the adhesion stress of the disc's middle three lamellar compartments on a smooth surface (Fig. S9E). The adhesion stresses decrease with the increase of the modulus of the ultra-soft layer both in air and under water. The maximum adhesion stresses of low-modulus lamellar compartments are the largest, increasing by 47% and 146% compared to middle-modulus and high-modulus lamellar compartments underwater, respectively. The biomimetic suction disc with the high-modulus ultra-soft layer cannot achieve adhesion in air.

We also performed experiments to track the internal pressure versus time of one lamellar compartment (Fig. S9F), which showed the influence of lamellae rotation on attachment performance. We found that when the lamellae become erect during disc attachment, the negative pressure of the lamellae compartments decreased by 45.8% (i.e., the pressure differential increased) without breaking the seal of the compartments (Fig. S9F). This result indicates that hydrostatically induced lamellae rotation positively influences redundant adhesion performance without breaking the overall seal.

Supplementary Text S4. Implementation of the aerial-aquatic robot

Based on the size and weight of the quadrotor robot, we selected 5-inch blades and 1900Kv brushless motors, which could ensure sufficient propulsion and flexibility for the robot in water and provide sufficient lift in the air. The robot control system consists of the flight control system, electronic governor, PPM encoder, low-frequency radio communication equipment, remote control, and battery. Figure S10A indicates the transmission process of the robot's control signal (green arrow) and power (red arrow). A radio frequency of 433MHz was chosen to support the communication need of the robot's aerial-aquatic work. The low-frequency receiver supports ten channels of PWM signal output, of which four channels connect the brushless motors to provide power for the robot. The remaining channels are used to extend the driven equipment, such as the three servos for driving the biomimetic disc motion. A control scheme with one proportional-integral-derivative (PID) is employed for the robot's motion control in both air and water. The servomotor, flight control system, electronic governor, PPM encoder, and low-frequency radio receiver are waterproofed with silicone rubber (704, Nanda, Nanjing, China) (Figs. S11 and S12). The battery and its plugs were also waterproofed with silicone rubber (704, Nanda, Nanjing, China). The brushless motors' plugs were carefully waterproofed by wrapping them with heat shrink tubing.

Supplementary Text S5. Transition of the aerial-aquatic robots

The main challenges affecting the transition process for rotor-wing robots are: the abrupt decrease in thrust when the propeller comes in contact with the water-air surface, and the rapid decrease in buoyancy as the vehicle emerges from the water surface. Thus, the propellers need to provide enough thrust underwater to expose the water-air surface and accelerate quickly in the air to achieve the target rotational speed, generating enough thrust to pull the entire robot out of the water. The propeller easily reaches the maximum rotational speed underwater. And for the robot to achieve the water-to-air transition, the propellers must reach a rotational speed to overcome gravity and hover in the air. Figs. 5F, 5G, and S14 show that the rotational speed intervals that self-folding, commercial, and fixed-unfolded propellers can achieve to transition are 1400~9600 rpm, 600~13300 rpm,

and 300~9600 rpm, respectively. The maximum difference between the rotational speed in air and water is 32 times (for the fixed propellers).

In a water tank (with a dimension of 110 × 80 × 70 cm), we measured the rotational speeds of the three propellers during the robot's transition from water (depth: 30 cm) to air (Fig. 5H, Fig. S15). High-speed camera images show three moments at the beginning, transition, and end of the process (Fig. S15). The propeller will reach its maximum underwater speed, accelerate at the water-air boundary, and then continue to accelerate rapidly out of the water after exceeding the gravitational equilibrium speed in the air. The robot's water-to-air transition process is determined by rotational speed difference, so a rapid decrease in propeller rotational speed difference is key.

Supplementary Text S6. Stability of water-air transition across a challenging water surface

There are two reasons for the stability of the robot's transition: the self-stabilization mode of the quadrotors assists this process. When the quadrotor is tilted, it can be leveled autonomously (Movie. S9). Due to the differing thrust forces of rotors in the water and air (larger in water and smaller in the air, Figs. 5F, 5G, and S14), the quadrotor will balance itself parallel to the water-air boundary by the thrust moment. Based on the above two features, the robot can smoothly transit wavy water surfaces and also cross the water-air surface if only two rotors are submerged.

Supplementary Text S7. Advantages of combining a redundant adhesion disc and an aerial-aquatic quadrotor

Robot with a combination of a redundant adhesion disc and an aerial-aquatic quadrotor has the following advantages:

Redundant disc adhesion requires preload, and the quadrotor can provide sufficient preload for the disc to adhere. Moreover, it can provide vertical, tilt (45°), horizontal, and other multi-directional preloads in air and water, which is difficult to achieve with other carriers (Movies S12, S14, S17, and S18).

The high maneuverability of the quadrotor itself allows the robot to work in complex environments (in the wild) and complete adhesion in narrow space (Movie S12, S19, and S20, Fig. 17H).

The aerial-aquatic quadcopter, as a typical device, can work in many wild environments, but also brings the problems of high energy consumption and short working time. The redundant adhesive disc's adaptability for multi-complex surfaces can let the quadcopter "hitchhiking", which improves the operating time and application range (Movie S13, S17, and S18).

The redundant disc reduces the operative difficulty and time of the aerial-aquatic quadrotor, when attaching challenging surfaces (Movie S12, Fig. S17A-F).

Supplementary Text S8. Power measurements for the aerial-aquatic hitchhiking robot

We measured the working time of the robot in hovering and hitchhiking (adhesive) states in air and under water until new fully charged Li-Po batteries became depleted. Under the same battery conditions, we also measured the robot's working time as it continuously transited the water-air boundary in a water tank (water depth of 20 cm). The average

power of the robot in hovering, hitchhiking, and transition states were calculated based on the energy of the battery.

Supplementary Text S9. Maximum hitchhiking speed of the aerial-aquatic robot

We calculated the drag coefficient to be approximately $c_d = 1.1$ through the measured flow speed and drag force:

$$F_d = \frac{1}{2}\rho v^2 c_d S \quad (5)$$

where F_d is the drag force, ρ is the water density, v is the flow speed, and S is the section area that faces the flow.

With equation (5), the maximum water flow that the robot can resist can be roughly calculated according to the maximum shear resistance force on a 50 μm surface in the water (F_d = 134.95 N, Fig. 4D; A = 13275.69 mm^2) as the maximum drag force F_d. As a result, we calculate that our bio-inspired disc could resist a maximum 4.3 m/s flow.

Supplementary Text S10. Adhesion experiments of the aerial-aquatic robots

The adhesion success rate experiment was conducted in a self-built circulating water tank with a total experimental area of about 80×60×40 cm. The water used in the experiment was artificially salinated to mimic seawater (3.5% salinity). The adhesion surface used in the experiment was an artificial acrylic board immersed in a natural pond during the season of vigorous microbial growth (from June to July) for approximately two months. The flow velocity of the circulating water tank was set to 0.5 m/s and an additional interference jet was added through a water pump with a flow of 3.13 m/s. In the above conditions the robot was maneuvered to attach to the surface. We tallied the adhesion successes and failures and calculated the success rate. The experimental process was repeated 22 times. The adhesion time of the robot was also measured experimentally in the circulating tank under the same conditions (saltwater, identical flow rates, with the pond-soaked acrylic surface). The robot initially attached to the surface and a 500 g weight was suspended from it as an external load. Then we started a timer and measured the adhesion time.

Supplementary Text S11. Adhesion experiments of the biomimetic disc prototypes

The pull-off force and frictional force were measured using a multiple-axis force transducer (Mini 40 F/T sensor, ATI Technologies Inc., USA) mounted to a robotic arm with a speed of 1 mm/s (MOTOMAN MH3F, YASKAWA Inc., Japan). All the experiments were completed in air and under water. We measured the frictional stress of four adhesive discs with 2, 4, 6, and 8 rows of lamellae formed 3, 5, 7, and 9 lamellar compartments, respectively, with a preload force (20 N), on a smooth surface. We also measured the frictional force of the fully functional biomimetic disc with hydrostatic enhancement; disc control without lamellae compliance; disc control without lamellae compartments; and disc with lamellae compartments and compliance, but without hydrostatic enhancement.

To explore the applicable surface roughness range of lamellar compartments, we tested adhesion stress of three middle compartments on a smooth surface (glass plate) and eight

rough surfaces (sandpaper, 3M, Inc.) with different roughnesses of 22, 50, 68, 100, 162, 201, 269, and 425 μm. To evaluate the contribution of the lamellar compartments in frictional force and attachment time, we fabricated two prototypes: one with sealed lamellar compartments and control with compartments connected by holes (to negate the effect of compartment adhesion).

Using these disc prototypes, we measured the frictional force on smooth and rough surfaces (R_a: 50, 201, 425, and 764 μm). We studied the maximum adhesion time of two prototypes on a rough surface (50 μm) under a 10 N and 30 N load using a mechanical testing machine (Zwick z0.5, Zwick/Roell Co., Ulm, Germany). We also tested the adhesion stress of the biomimetic disc on smooth and rough surfaces (R_a: 50, 201, 425, and 764 μm). To investigate the adhesive performance of the disc on curved surfaces, we tested the adhesion stress of the disc on smooth surfaces with varying curvatures (curvature radius: 20, 35, 50, 75 cm) and on one rough curved surface (R_a = 50 μm, curvature radius: 50 cm).

Tables:

Table S1. Comparison of the performance of aerial-aquatic robots. ("‡" represents no results or no data presented in the papers.)

Robots (reference)	High maneuverability	Untethered	Consecutive transition	Transition time (s) (water-to-air)	Stability during the transition (inclination angles are less than 10°)	Attachment ability
Aerial-aquatic hitchhiking robot	**Yes (quadrotor)**	**Yes**	**Yes**	**0.35 s**	**Yes**	**Yes**
Flapping wing aerial-aquatic robot (*18*)	Yes (flapping-wing flight)	No	‡	129 s (Collection and combustion processes)	‡	No
Aquatic jump-gliding robot (*15*)	No (jump-gliding flight)	Yes	Yes	865 s (Collection and combustion processes)	‡	No
Fixed-wing robot (*13*)	No	Yes	‡	1.89 s (Attitude adjustment time is not included)	‡	No
Bio-inspired flying squid robot (*17*)	No	Yes	‡	About 4 s (Water supplement and propulsion)	‡	No
Eight-rotor robot (*19*)	Yes	No	Yes	About 1.53 s	‡	No
Loon Copter (*20*)	Yes (quadrotor)	Yes	‡	About 13 s	No	No
MHAUV (*22*)	Yes	Yes	‡	About 30.0 s	‡	No

Table S2. Comparison of the redundant and non-redundant adhesive biomimetic discs

Features/Functional performances	Previous biomimetic remora disc (*36*)	This work
Soft lip, lamellae and spinules	Yes	Yes
Artificial connective tissue	No	Yes
Oblique lamellae	No	Yes
Disc flexibility	No	Yes
Redundant adhesion	No	Yes
Attachment	Yes	Yes
Detachment	Through external water injection to balance pressure differential	Through an onboard servo actuator
Lamellae actuation	Through six external pneumatic actuators	Through an onboard hydraulic actuator
Surfaces that can be attached	Flat/rough	Curved/incomplete/biofouling/ rough
Achieved maximum roughness of surfaces	200 μm	769 μm
Air/water adhesion	Underwater only	Air and underwater
Tethered/Untethered	Tethered	Untethered
Adhesion time	Not tested	2944.4 ± 143.7 minutes
Frictional stress	4.9 ± 0.1 kPa	42.9 ± 2.1 kPa

Supplementary figures:

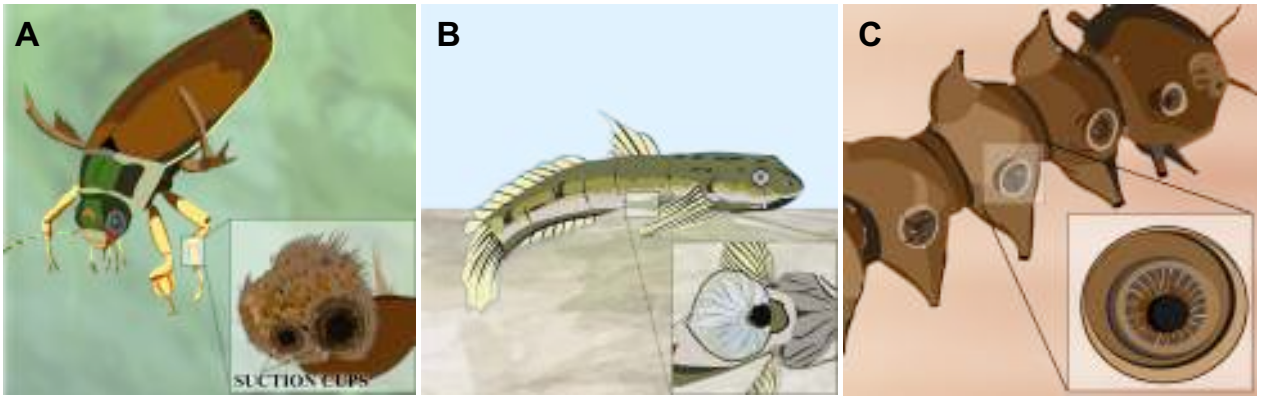

Fig. S1. Examples of multi-terrain biological suction-based attachment systems. (A) Male diving beetles (*Dytiscinae*) utilize passive circular sucker structures on their feet during underwater mating. **(B)** Waterfall climbing goby fishes (*Gobiesox*) utilize a pectoral suctorial organ that enables them to maintain adhesion even while climbing vertical surfaces. **(C)** Net-winged midge larvae (*Blephariceridae*) highlight multiple active ventral suckers on their body segments to locomote in torrential water streams.

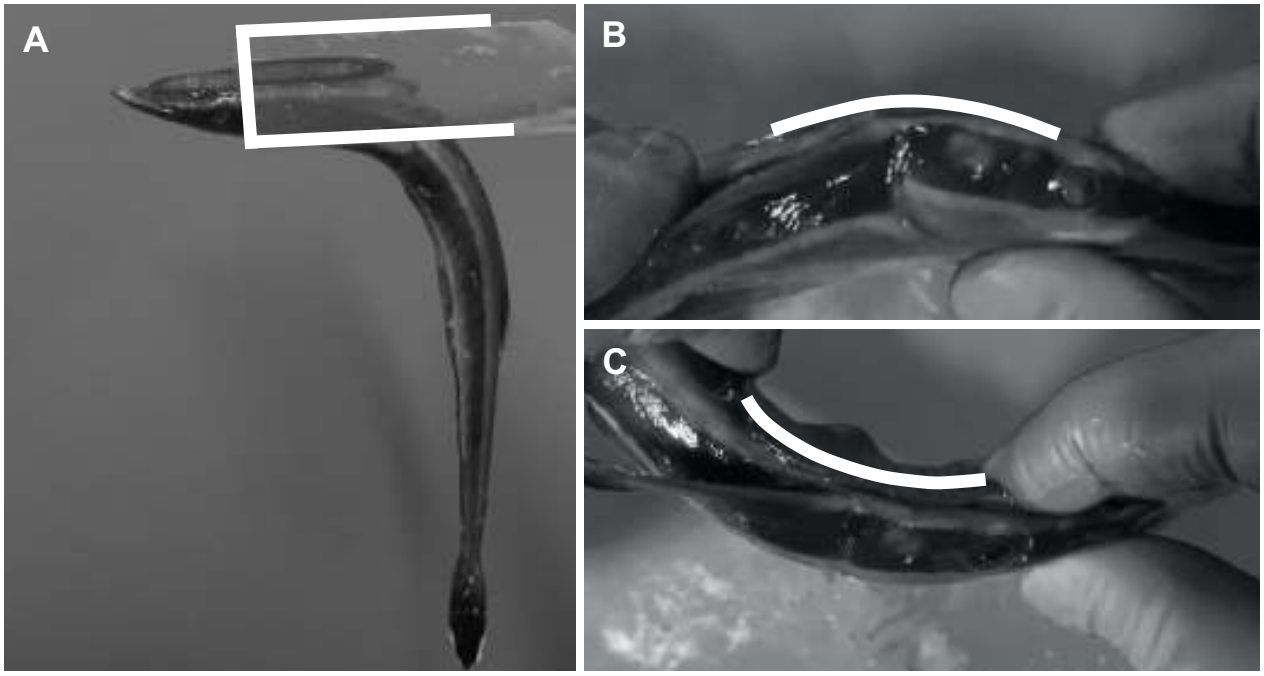

Fig. S2. Redundant adhesion and flexibility of the remora adhesive disc. (A) An anesthetized remora can firmly attach to a glass substrate using one-half of its disc (hanging in the air). The adhesive disc of remora can bend in the dorsal **(B)** and ventral **(C)** directions. We highlight the profiles (solid white) along the midline of the disc.

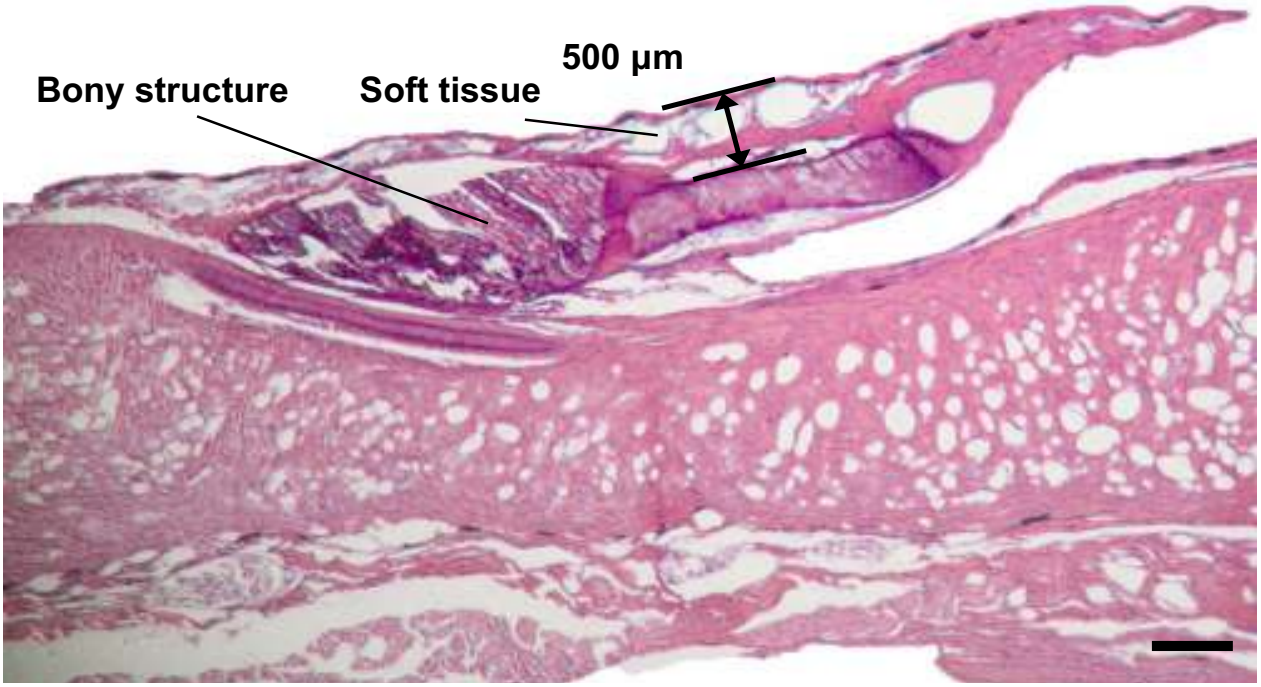

Fig. S3. Histology image of the cross-sections of remora's lamellae. For histological investigation, the lamellae of a remora disc were fixed in 4% paraformaldehyde/PBS over 24 h, then were paraffin-embedded, sectioned, and stained by hematoxylin and eosin (HE staining). Tissue sections were scanned using an optical microscope (XSP-12CA, Shanghai Optical Instrument Factory Co., Shanghai, China). The scale bar is 500 μm.

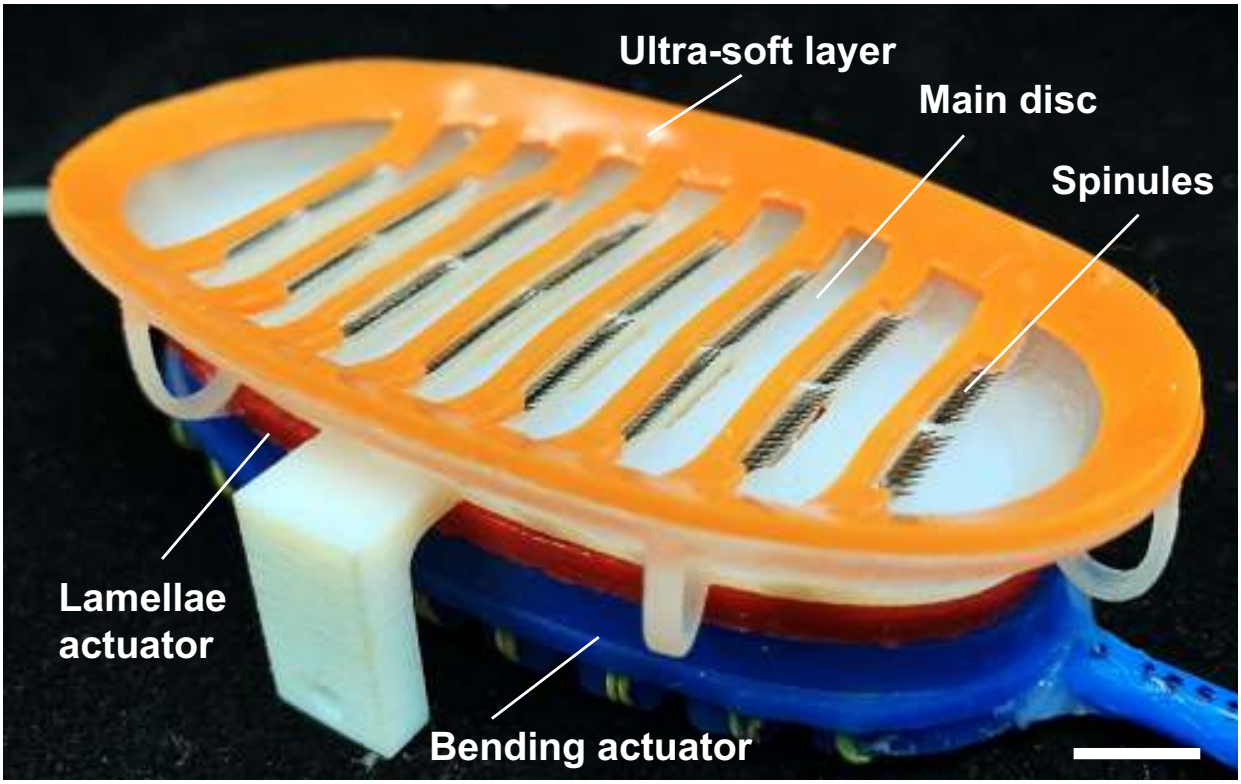

Fig. S4. Biomimetic remora disc prototype. The scale bar is 1 cm.

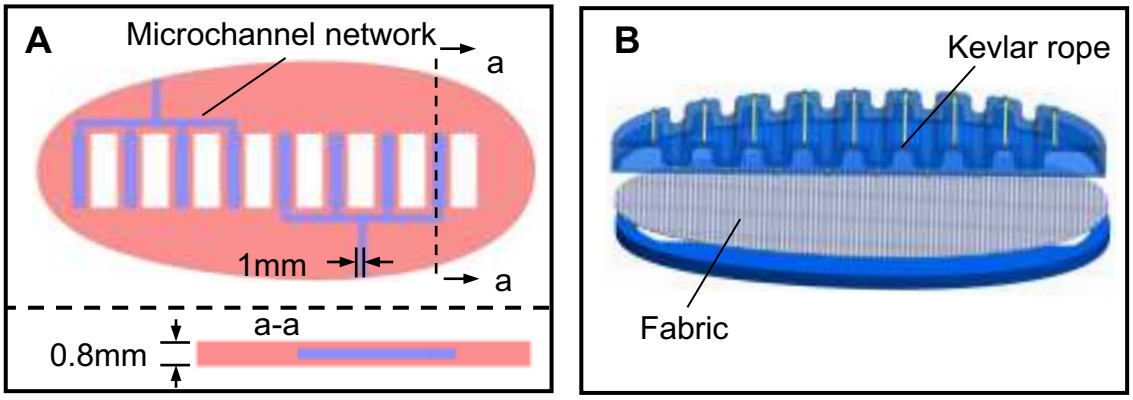

Fig. S5. Design of the lamellae actuator (A) and bending actuator (B).

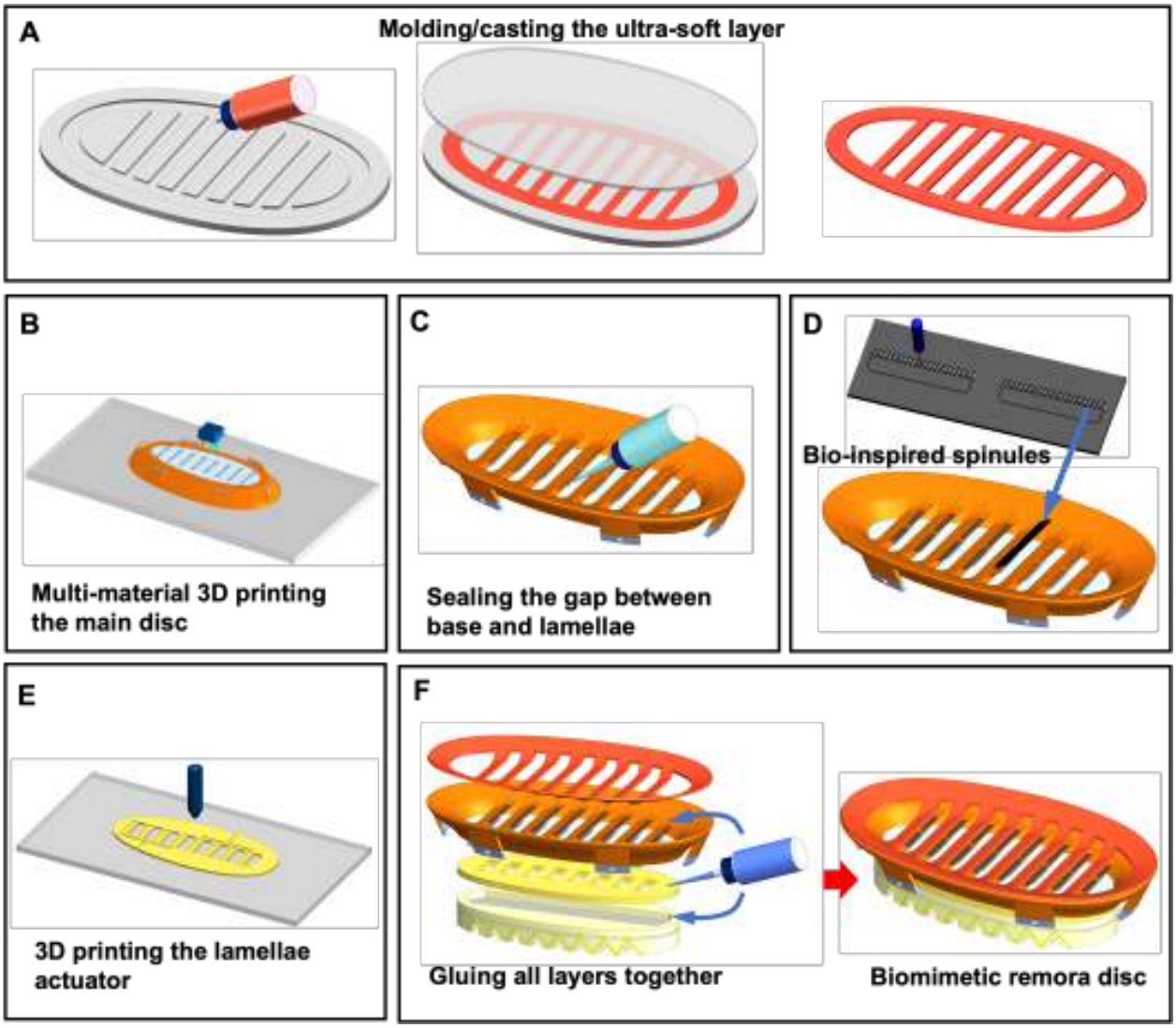

Fig. S6. Fabrication of the remora disc prototype. (A) Molding/casting the ultra-soft layer with soft silicone rubber (Ecoflex 10, Smooth-on, Inc, Easton Pa, USA). **(B)** The main disc's remaining components were fabricated with a multi-material 3D printer Objet Connex C3 (Stratasys Ltd, Eden Prairie, MN, USA). **(C)** Sealing both sides of the disc (along the gap between the flexible base and lamellae) with soft silicone rubber (Ecoflex 10, Smooth-on, Inc, Easton Pa, USA). **(D)** Fabrication of the bio-inspired spinules. The spinules were fabricated by cutting 200 μm plates made from stainless steel (Stainless steel 301, Shanxi Taigang Stainless Steel Co Ltd., Shanxi, China). We used a 355 nm diode-pumped solid-state laser micromachining system (DC150H-355, Photonics Industries International Inc., NY, USA) to cut the stainless steel into spinule patterns. Then we glued rows of spinules to the lamellae with 502 instant adhesives (No. 7147, Deli Group Ltd. Zhejiang, China). **(E)** The lamellae actuator was printed using silicone materials with a 3D printer (ACEO @ Silicone GP, Wacker Chemie AG, Germany). **(F)** Gluing all layers together with a silicone rubber adhesive (Sil-Poxy, Smooth-on, Inc, Easton Pa, USA).

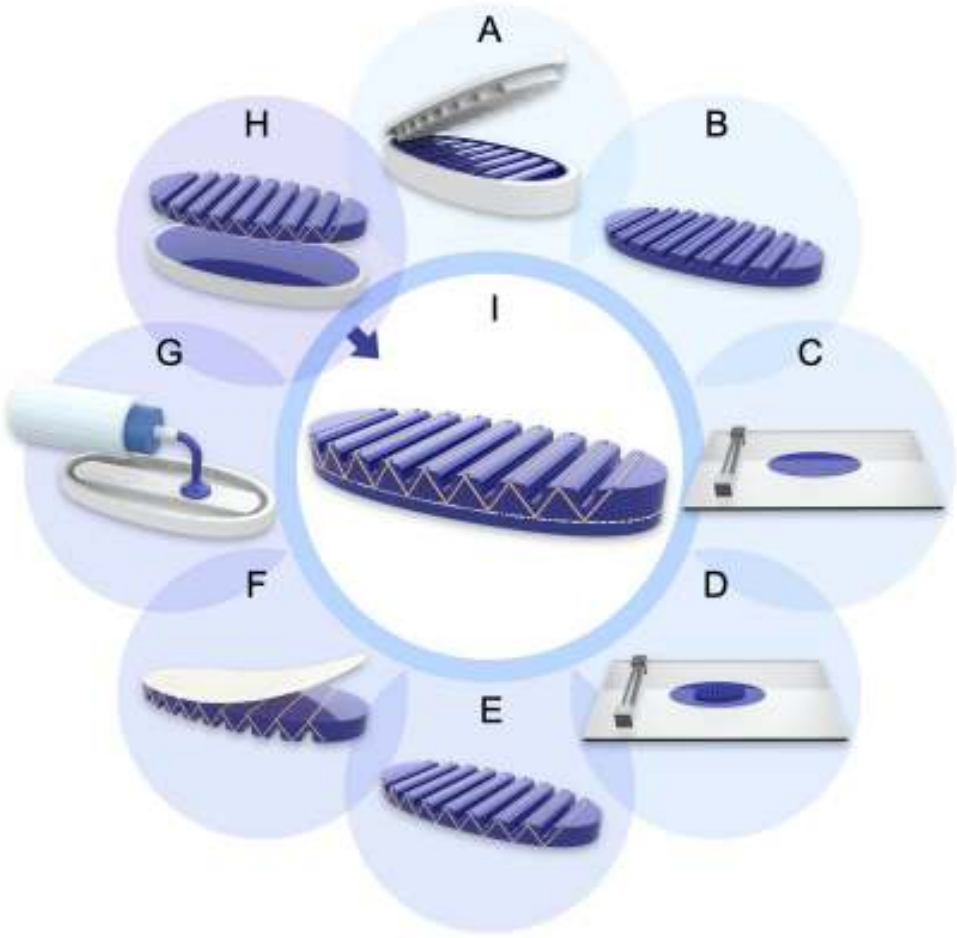

Fig. S7. Fabrication of the bending actuator. (A) The upper shell of the bending actuator was obtained by molding/casting (Mold Star 30, Smooth-on, Inc, Easton Pa, USA). **(B)** The upper shell of the bending actuator was obtained. **(C)** Using a scraper to scrape a 1 mm thick silicone film (Mold Star 30, Smooth-on, Inc, Easton Pa, USA). **(D)** Putting the upper shell on the film before the film cured. **(E)** Wrapping Kevlar wire around the drive for reinforcement **(F)** A textured layer (polyester fabric, Liangyi Textile New Material Co., LTD, China) is added to enhance unilateral modulus. **(G)** The lower shell of the bending actuator was obtained by molding/casting (Mold Star 30, Smooth-on, Inc, Easton Pa, USA). **(H)** Gluing the upper actuator and the lower shell together through secondary pouring (Mold Star 30, Smooth-on, Inc, Easton Pa, USA). **(I)** Bending actuator prototype.

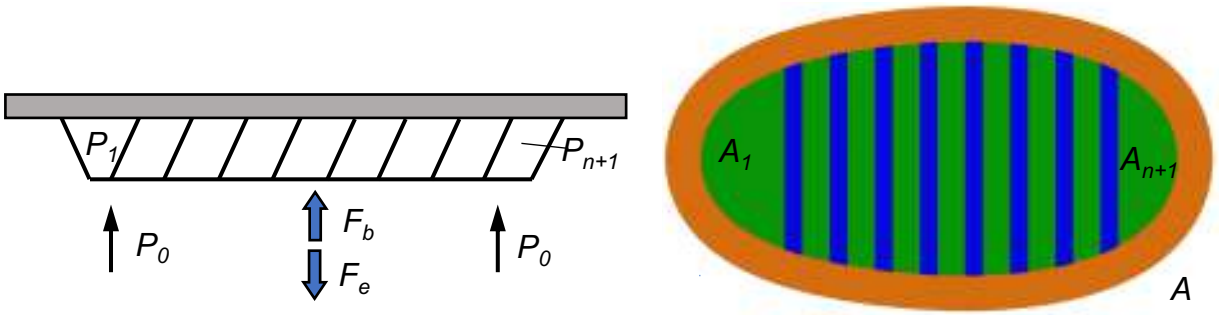

Fig. S8. Simplified model of the remora disc. P_0 represents the environmental fluid pressure, A represents the area of the disc pad, P_k represents the internal pressure of the lamellar compartment, A_k represents the area of the lamellar compartment, n represents the number of lamellae in the disc, and F_e represents the external load. F_b represents the resultant force of gravity and (negligible) buoyancy of the disc.

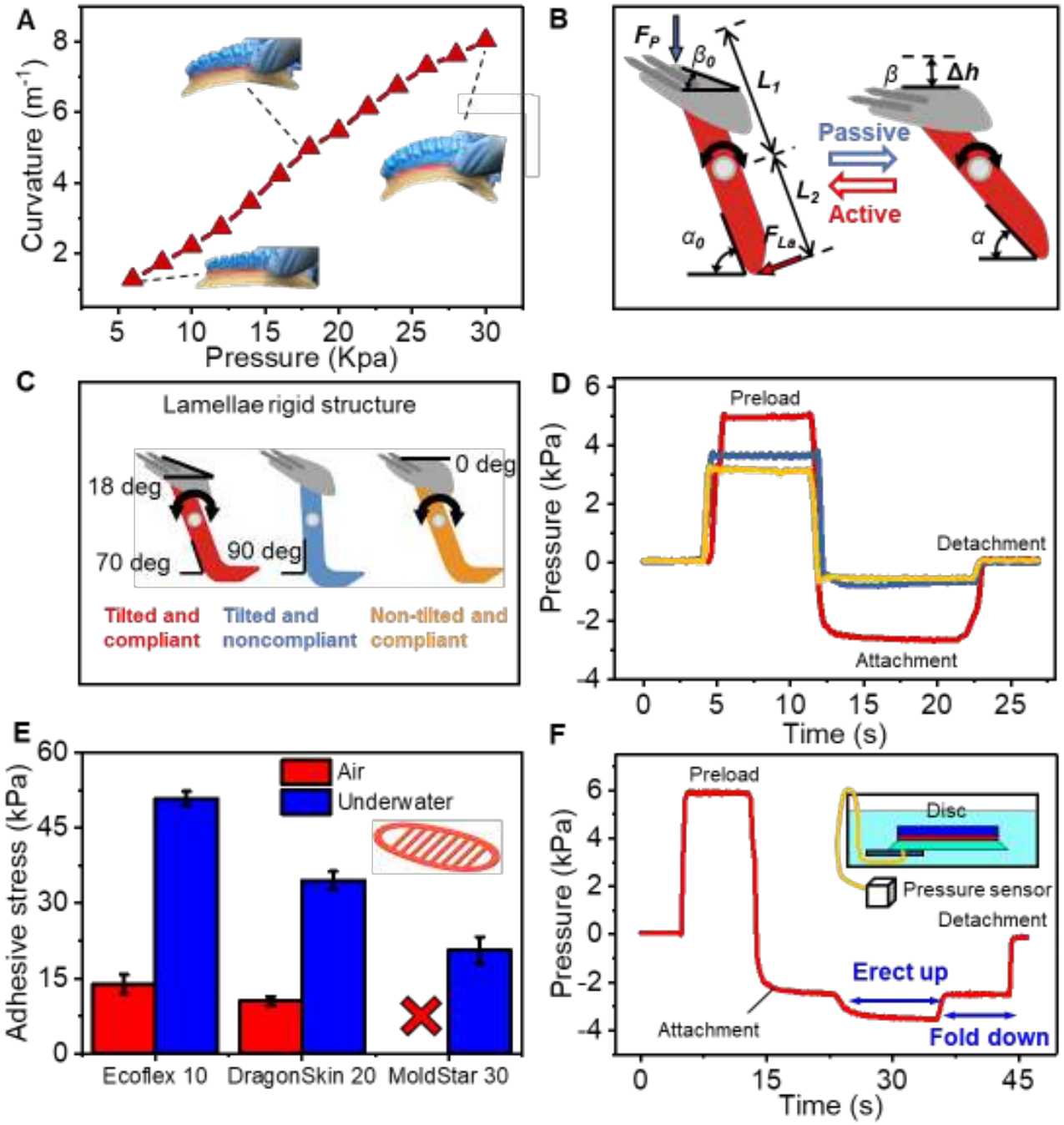

Fig. S9. The performance of the biomimetic disc prototype. (A) The curvature of the disc prototype under different bending pressures. **(B)** Mechanical model for passive and active rotation of the lamellae. **(C)** Biomimetic lamellae (red) have a tilted top with a compliant joint for rotation like their biological counterparts. For comparison, we also fabricated a disc with tilted but noncompliant lamellae (blue) and a disc with non-tilted (flat) but compliant lamellae (yellow). **(D)** Fully submerged underwater measurements of the internal pressure of different biomimetic discs with three types of lamellae (preload: 10 N). **(E)** The maximum adhesion stress of the disc's three lamellar compartments (the mid-portion of the disc) with different materials attaching to a smooth surface both in air and under water ($N = 5$). The red X represents adhesion failure. **(F)** Internal pressure vs. time of one lamellar compartment of the disc. Erecting the lamellae further reduced the negative pressure (increased the pressure differential) without breaking the seal of lamellar compartments. Error bars represent ± 1 SD.

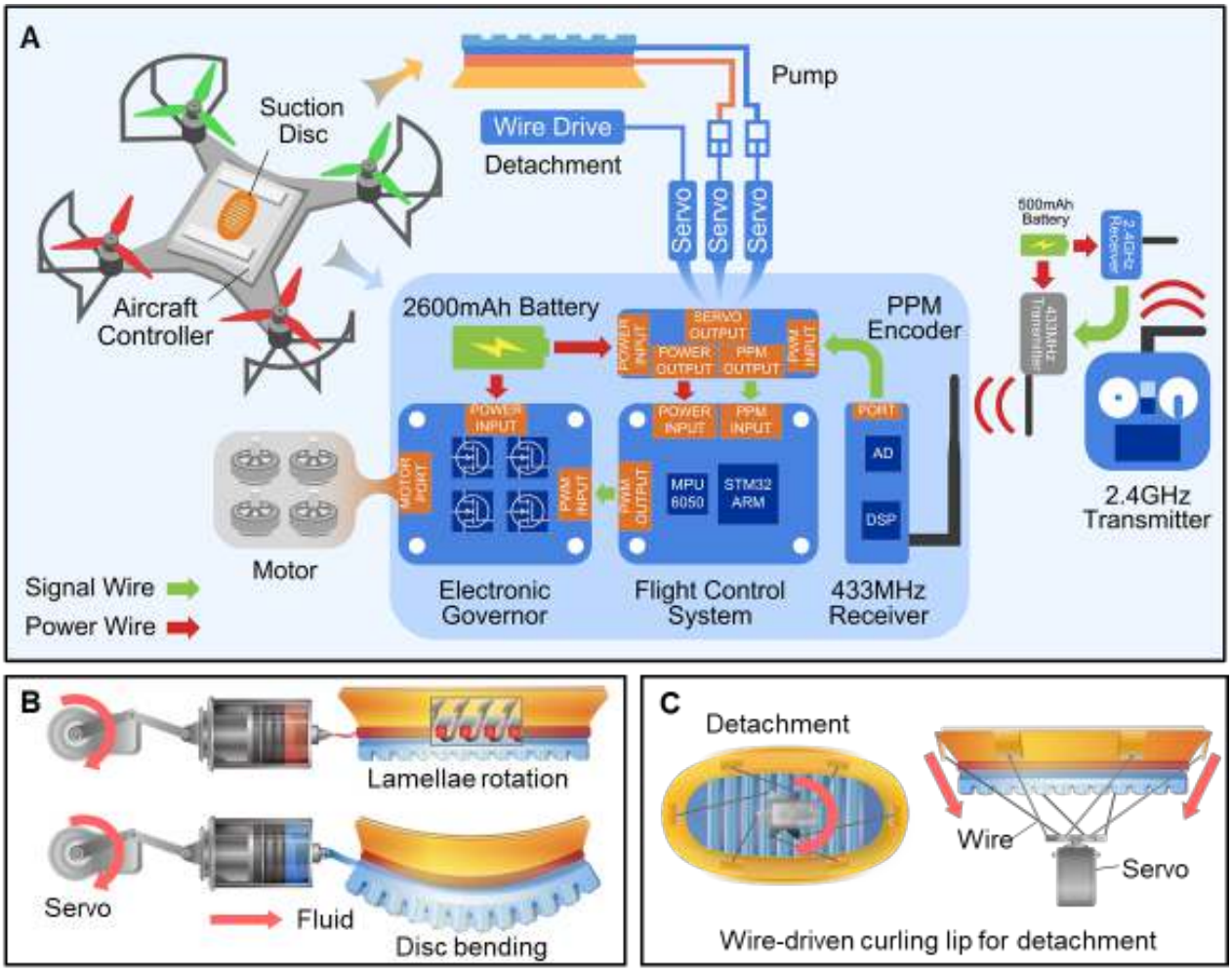

Fig. S10. Robotic system and actuation method of the adhesive disc. (A) The system diagram of the onboard electronics for control and actuation and the power supply for the robot. **(B)** Two lightweight hydraulic pumps (25 g each) were applied to actuate the lamellae rotation (for frictional enhancement) and to bend the disc (for attaching to curved surfaces). **(C)** A cable-driven mechanism was applied to curl the peripheral soft lip to break the seal for rapid detachment.

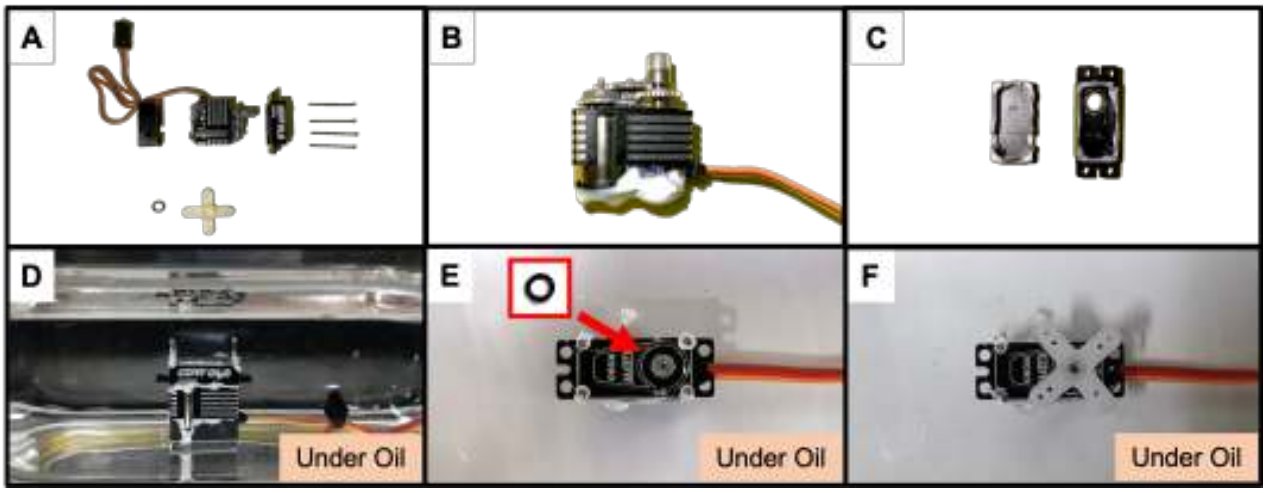

Fig. S11. Waterproofing steps of a servomotor. (A) Disassemble the servomotor. **(B)** Apply silicone rubber (704, Nanda, Nanjing, China) to waterproof the circuit board. **(C)** Apply 704 on the assembly edges. **(D)** Assemble the servomotor under insulating oil to prevent freshwater/seawater infiltration. **(E)** Put an O-ring on the output shaft of the servomotor. **(F)** Press on a servomotor arm to fix the O-ring for sealing.

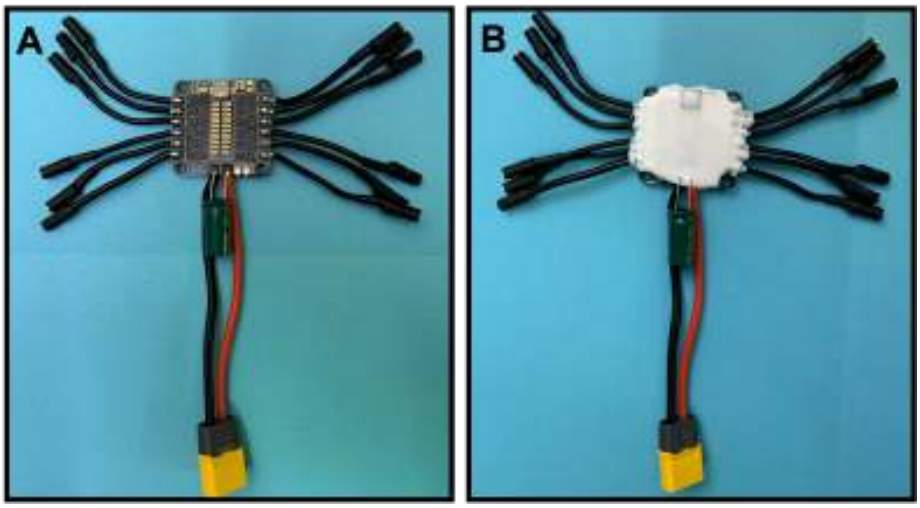

Fig. S12. Waterproofing steps of the electronic components. (A) Initial components. **(B)** Coating in silicone rubber (704, Nanda, Nanjing, China) to waterproof the circuit board and the joints.

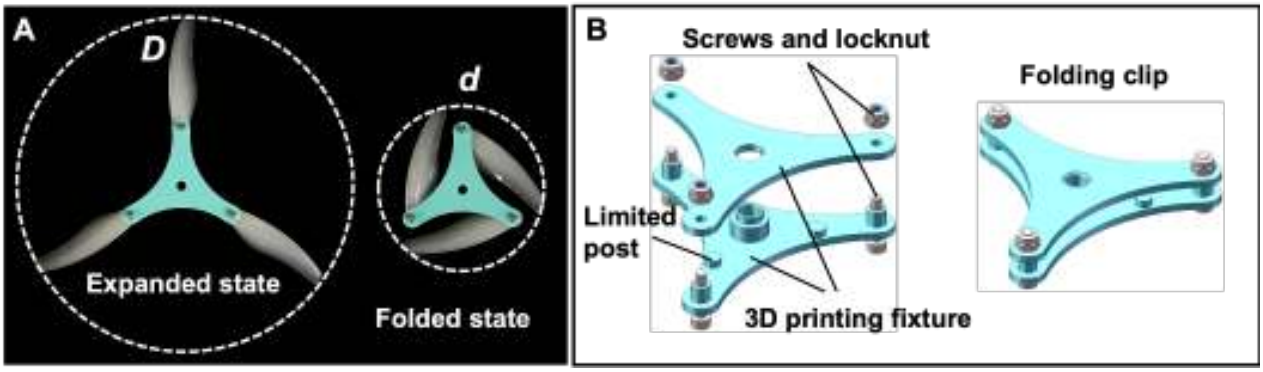

Fig. S13. Passive morphing propeller design. (A) The self-folding propeller consists of a folding clip (blue) and 5-inch blades (white). The propeller's diameter in an unfolded state (*D*) and folded state (*d*) are 170 mm and 85 mm, respectively. The folding ratio (*D/d*) is 2. **(B)** The custom 3D-printed folding clip. Three posts restrict the folded blades from further folding.

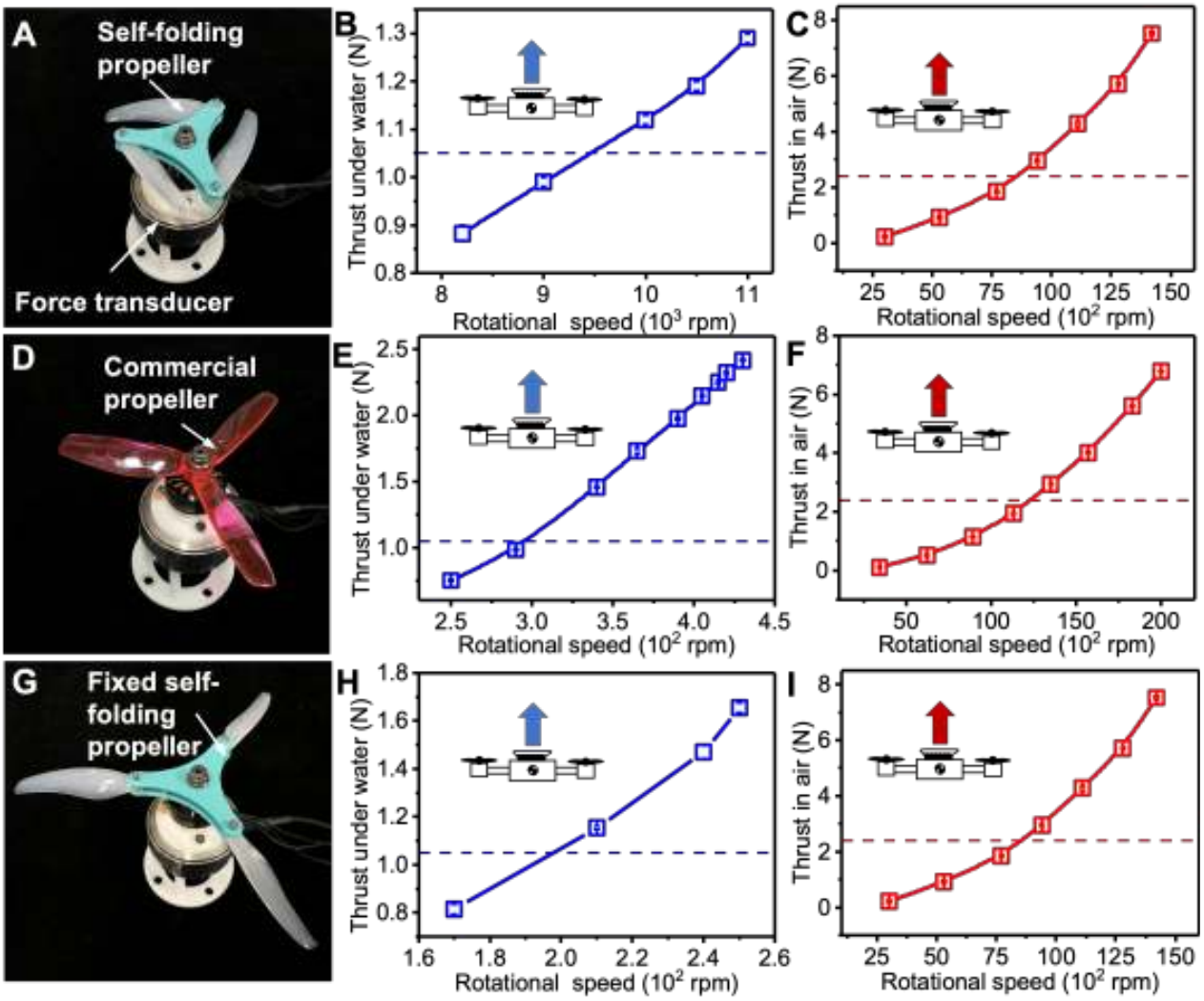

Fig. S14. Rotor force vs. speed both in air and under water. Testing the thrust of a self-folding propeller (**A**), a commercial propeller **(D),** and a self-folding propeller in an unfolded state **(G)** at different rotational speeds with a six-axis force sensor both in air and underwater. Thrust vs. rotational speed for the self-folding propeller in air (**B**) and water (**C**), for the commercial propeller in air (**E**) and water (**F**), and the fixed-unfolded propeller in air (**H**) and water (**I**). When the rotational speed of the propeller exceeds the critical speed (marked by a dashed line), the robot moves upward under water (blue dashed line) or flies up in air (red dashed line). Error bars represent ± 1 SD.

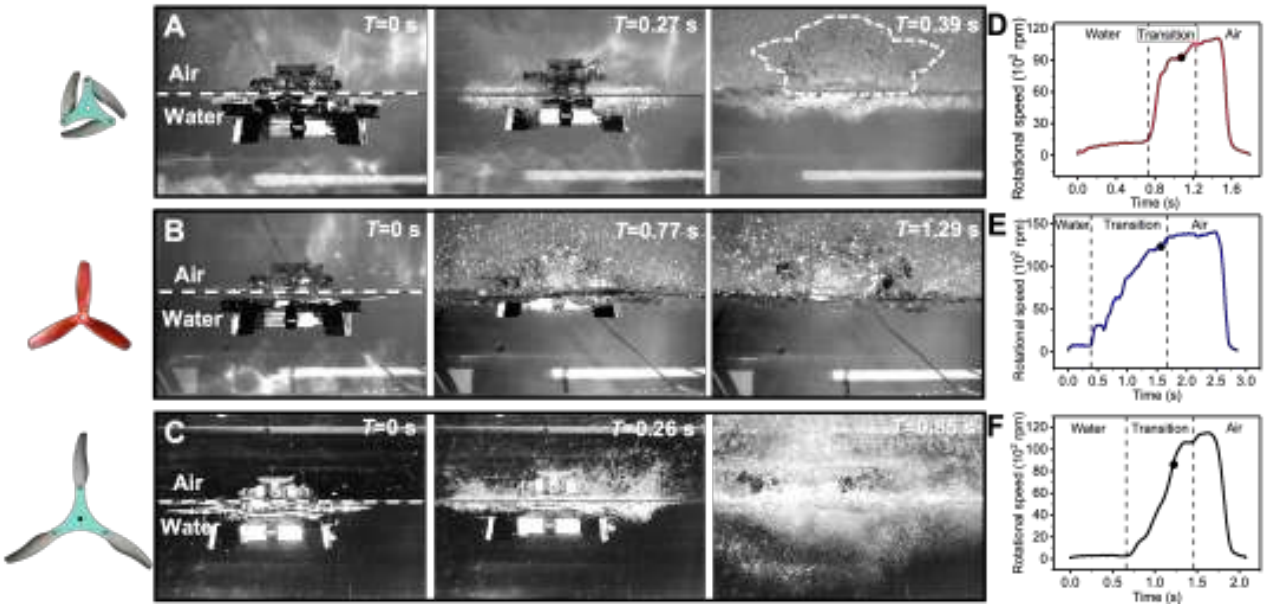

Fig. S15. Robot transition and propeller speed vs. time during the transition. Images of the robot with self-folding propellers **(A)**, commercial propellers (**B**), and fixed-unfolded propellers **(C)** taking off from the water at various time instants in a laboratory water tank. The average rotational speed and total transit time of the different propellers vary across propeller configurations. (**D-F**) The range between the two black dashed lines is the boundary transition period.

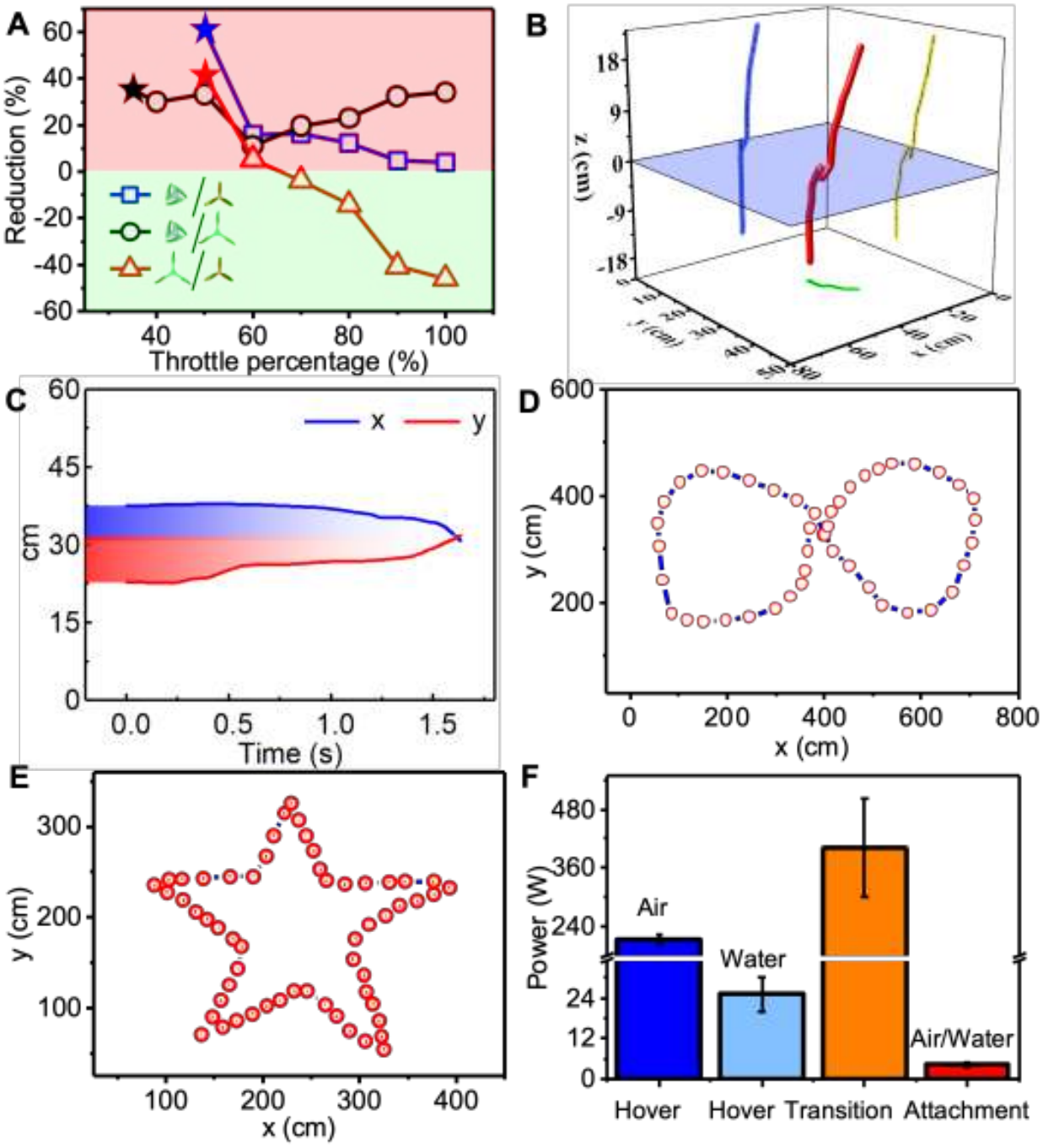

Fig. S16. Water/air transition, movement, and adhesion performance of the robot. (A) Transition time ratios between each of the three propeller configurations vs. throttle percentage. **(B)** Transition trajectories of the robot from water to air in a three-dimensional view. The profiles were constructed from high-speed images (250 fps) and then calculated in MATLAB. **(C)** The x and y trajectories of the robot versus time during the water-to-air transition. Underwater navigation "figure eight" **(D)** and "pentagram" **(E)** trajectories of the robot under remote control. **(F)** Power consumption of the hitchhiking robot in hovering, attached, and transitioning states (in air and under water). Error bars represent ± 1 SD.

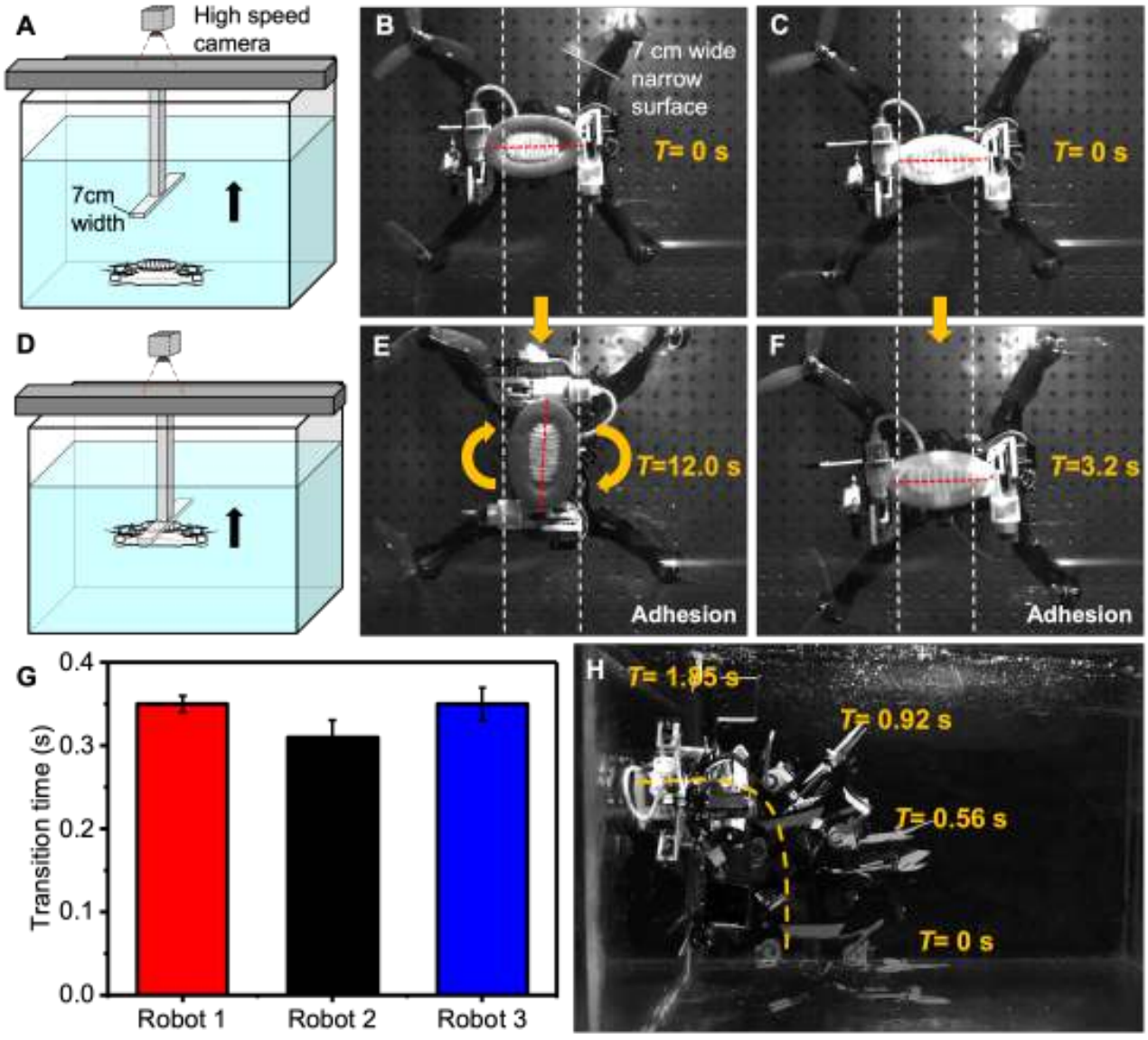

Fig. S17. Advantages of combining a redundant adhesion disc and an aerial-aquatic quadrotor. Schematic of the experimental setup at the initial state **(A)** and at the adhesion state **(D)**. The whole setup includes a 110 × 80 × 70 cm water tank, a high-speed camera, a 7 cm wide acrylic plate (size smaller than the long axis of the suction disc), and two aerial-aquatic robots. The initial position of the robot with a non-redundant adhesive disc (*36*) **(B)** the initial position of the robot with a redundant adhesive disc **(C)** The axis of the suction discs (red dotted line) and the edge of the plate (white dotted line) are perpendicular. (E-F) shows the adhesion states of two robots. **(E)** The robot with the non-redundant adhesive disc needs to rotate 90° before it can attach to the narrow surface, which takes 12.0 s. **(F)** The robot with the redundant adhesive disc is able to attach directly and quickly to the surface, taking only 3.2 s. **(G)** Effect of the equipped bioinspired adhesive disc on robot transition time. Three aerial-aquatic robots were built. Robot 1 is a robot equipped with a bioinspired adhesive disc and related onboard system (total mass: 950 g); robot 2 is a robot without a disc and its related onboard system (total mass: 716 g); and robot 3 is a robot without a disc but equipped with an added load to make the total mass equal to that of robot 1. There was no noticeable difference in the transition time between robot 1 (with a disc) and robot 3 (without a disc), which had the same mass. Error bars represent ± 1 SD. **(H)** The robot can complete vertical sidewall adhesion in a narrow space.

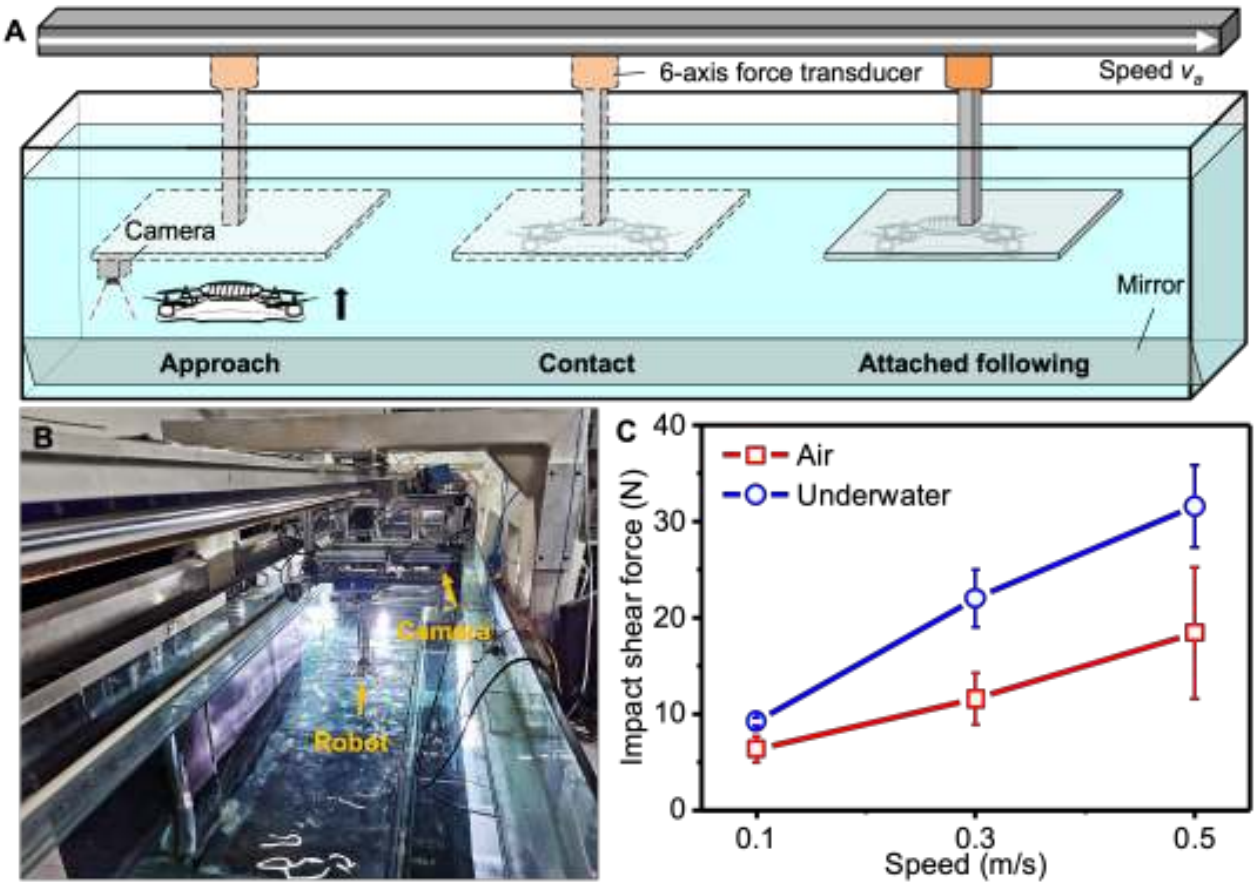

Fig. S18. Hitchhiking experiments in air and water. (A) Schematic of the experimental setup. The whole setup can be divided into three parts: instantaneous self-propelled guide rail, data acquisition systems (a six-axis force sensor and high-speed camera), and the aerial-aquatic robot. Note that the high-speed camera is fixed to the guide rail and takes a side view of the entire hitchhiking process via a mirror placed at 45 deg. **(B)** Photograph of the towing tank with the size 7.8×1.2×1.1 m. **(C)** Relationship between the impact shear force on the adhesion surface and the relative velocity during the contact stage of the hitchhiking process in air (red) and water (blue). Error bars represent ± 1 SD.

Fig. S19. High-speed video demonstrates that the robot can achieve hitchhiking with only half of the disc attached because of redundant adhesion (A-C).

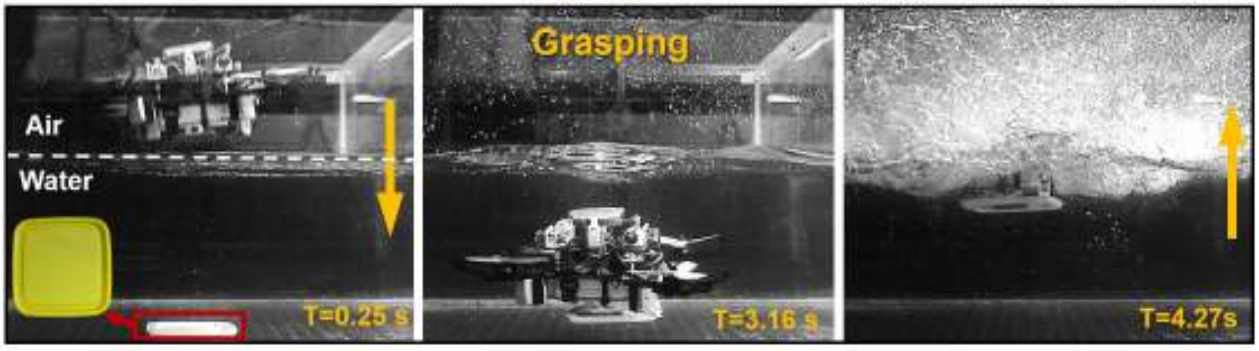

Fig. S20. High-speed images of the robot (with a biomimetic disc mounted underneath) transiting into water, grasping an object, and removing the object from the water.

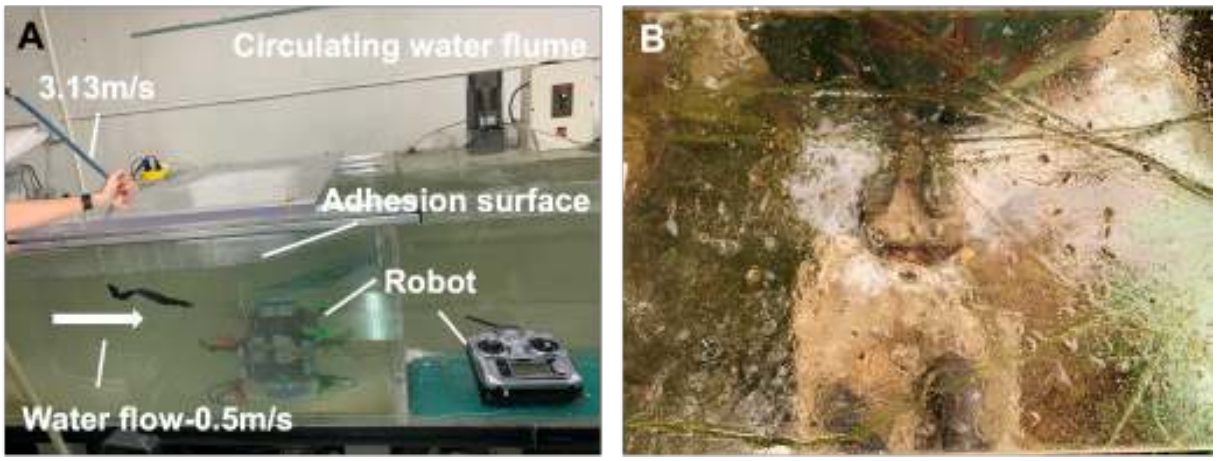

Fig. S21. The experimental device (A) and the artificial slippery surface (B) for the adhesion success rate and adhesion duration experiments. The scale bar is 1 cm.

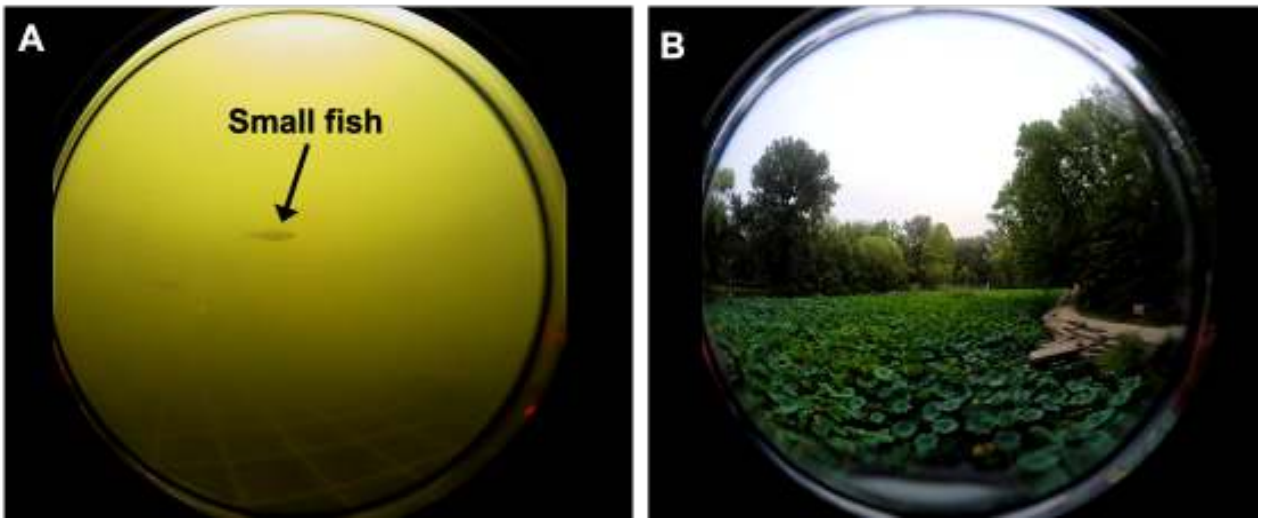

Fig. S22. The underwater (A) and aerial (B) images from the onboard camera.

Fig. S23. The rough rock to which the robot attached (Fig. 7D and the Movie S18).

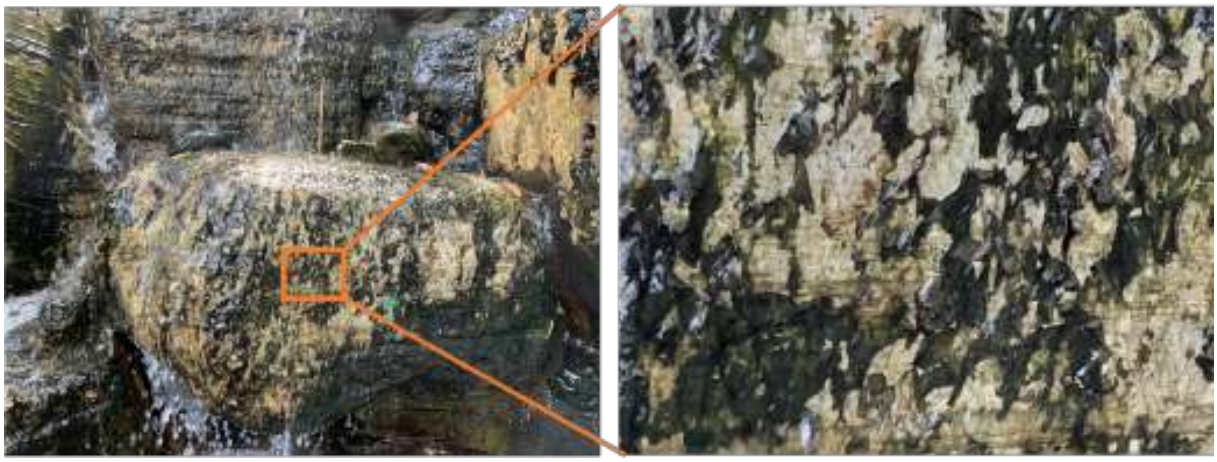

Fig. S24. Wet and slippery rock surface adhered to by the robot. The scale bar is 10 cm.

Fig. S25. Underwater images of the 10-15 m seabed from the onboard camera.